

Summer 2014

# Weld pool and keyhole dynamic analysis based on visual system and neural network during laser keyhole welding

Masiyang Luo  
*Purdue University*

Follow this and additional works at: [https://docs.lib.purdue.edu/open\\_access\\_theses](https://docs.lib.purdue.edu/open_access_theses)



Part of the [Mechanical Engineering Commons](#)

---

## Recommended Citation

Luo, Masiyang, "Weld pool and keyhole dynamic analysis based on visual system and neural network during laser keyhole welding" (2014). *Open Access Theses*. 652.  
[https://docs.lib.purdue.edu/open\\_access\\_theses/652](https://docs.lib.purdue.edu/open_access_theses/652)

This document has been made available through Purdue e-Pubs, a service of the Purdue University Libraries. Please contact [epubs@purdue.edu](mailto:epubs@purdue.edu) for additional information.

**PURDUE UNIVERSITY  
GRADUATE SCHOOL  
Thesis/Dissertation Acceptance**

This is to certify that the thesis/dissertation prepared

By Masiyang Luo

Entitled Weld Pool and Keyhole Dynamic Analysis Based on Visual System and Neural Network during Laser Keyhole Welding

For the degree of Master of Science in Engineering

Is approved by the final examining committee:

YUNG C. SHIN

PETER H. MECKL

GALEN B. KING

To the best of my knowledge and as understood by the student in the *Thesis/Dissertation Agreement, Publication Delay, and Certification/Disclaimer (Graduate School Form 32)*, this thesis/dissertation adheres to the provisions of Purdue University's "Policy on Integrity in Research" and the use of copyrighted material.

Yung C. Shin

Approved by Major Professor(s): \_\_\_\_\_

Approved by: David C. Anderson

07/08/2014

Head of the Department Graduate Program

Date



WELD POOL AND KEYHOLE DYNAMIC ANALYSIS BASED ON VISUAL  
SYSTEM AND NEURAL NETWORK DURING LASER KEYHOLE WELDING

A Thesis

Submitted to the Faculty

of

Purdue University

by

Masiyang Luo

In Partial Fulfillment of the

Requirements for the Degree

of

Master of Science in Engineering

August 2014

Purdue University

West Lafayette, Indiana

## ACKNOWLEDGEMENTS

I would like to express my special appreciation and gratitude to my advisor Dr. Yung C. Shin, who has been a tremendous mentor for me. I would like to thank you for giving me many instructions and guidance in my research work and encouraging me to move forward when I got stuck in difficulties. Your advice on both my research as well as my career have been priceless.

I would also like to thank my committee members, Dr. Peter Meckl and Dr. Galen B. King for serving as my committee members. I also want to thank you for your brilliant comments and suggestions, and for taking your time reviewing my thesis. I would also like to thank my labmates, Wenda Tan, Neil Bailey, Kyung-min Hong and Phuong Ngo. All of you not only helped me conduct the laser welding experiments but also shared your deep understandings of laser modeling work.

At the end, special thanks to my family. Words cannot express how grateful I am to my mother, father, grandmother and fiancée. Your support was what sustained me thus far. I also appreciate all the help of my friends who supported me to strive towards my goal.

## TABLE OF CONTENTS

	Page
LIST OF TABLES .....	v
LIST OF FIGURES .....	vi
ABSTRACT .....	ix
CHAPTER 1. INTRODUCTION .....	1
1.1. Motivation and Literature Review .....	1
1.1.1. Keyhole Laser Welding .....	1
1.1.2. Numerical Model Simulation of Laser Welding .....	2
1.1.3. Weld Pool Monitoring .....	5
1.1.4. Observation of Keyhole Dynamics .....	8
1.1.5. Neural Network Based System Identification and State Observer Design .....	11
1.2. Objectives of Thesis .....	13
1.3. Overview of Thesis .....	14
CHAPTER 2. EXTRACTION OF WELD POOL BOUNDARY .....	15
2.1. Experimental Setup .....	15
2.2. Boundary Extraction and Width Measurement .....	20
2.2.1. Analysis of image signal .....	21
2.2.2. Keyhole Extraction and Central Line Location .....	23
2.2.3. Weld Pool Boundary Extraction for Tail Part .....	25
2.2.4. Weld Pool Boundary Extraction for Head Part .....	31
2.2.5. Weld Pool Boundary Extraction for Middle Part .....	33
2.2.6. Weld Pool Width Measurement .....	34
2.3. Validation of Extracted Weld Pool Boundary .....	35
CHAPTER 3. ESTIMATION OF KEYHOLE GEOMETRY AND PREDICTION OF WELDING DEFECTS .....	45
3.1. Methodology of Estimating Keyhole Dynamics .....	45

	Page
3.1.1. Radial Basis Function Neural Network.....	45
3.1.2. Static RBFNN for Keyhole Dynamic .....	47
3.2. Data Collection and Static Neural Network Training .....	53
3.2.1. Detected Keyhole Diameters.....	54
3.2.2. Penetration Depth and Inclination Angle .....	56
3.2.3. Training Results of Static RBFNN .....	58
3.2.4. Testing of Static Neural Network .....	59
3.3. Dynamic RBFNN-based Observer for Keyhole Dynamic.....	61
3.3.1. Data Training for Dynamic RBFNN .....	61
3.3.2. Estimation Results of Dynamic RBFNN Observer .....	63
3.4. Prediction of Welding Defects .....	65
CHAPTER 4. CONCLUSION AND RECOMMENDATION OF FUTURE WORK.....	73
4.1. Conclusion.....	73
4.2. Recommendation of Future Work.....	74
LIST OF REFERENCES.....	76
VITA.....	80

## LIST OF TABLES

Table	Page
Table 2.1. Description of IPG YLS-1000 fiber laser .....	16
Table 2.2. Chemical composition of stainless steel 304.....	16
Table 2.3. Average of weld pool width.....	37
Table 2.4. Chemical composition of magnesium alloy AZ31B.....	42
Table 3.1. Designed experiments.....	53
Table 3.2. Average keyhole diameters from images.....	55
Table 3.3. Test data for penetration depth.....	60
Table 3.4. Test data for inclination angle.....	60
Table 3.5. Designed experiment parameters for stainless steel.....	68
Table 3.6. Designed experiment parameters for magnesium alloys.....	68



## LIST OF FIGURES

Figure	Page
Figure 1.1. Schematic of keyhole welding.....	2
Figure 1.2. Coaxial monitoring system with coaxial illumination.....	7
Figure 1.3. Captured weld pool image and extracted weld pool boundary.....	8
Figure 1.4. Collected data for inclination angle and penetration depth with different welding conditions (for four different focal spot diameters: 125 and 200 $\mu\text{m}$ (4 kW, Nd–Yag laser), 600 and 1000 $\mu\text{m}$ (4 and 6.3kW, diode laser)).....	9
Figure 1.5. Detection of welding porosities and bubbles of using X-ray imaging system...10	10
Figure 2.1. Photo of coaxial monitoring system and Mazak Controller.....	17
Figure 2.2. Coaxial visual monitoring system.....	17
Figure 2.3. Relative sensitivity response of CMOS camera used.....	19
Figure 2.4. Plasma spectrum in keyhole welding.....	19
Figure 2.5. Original images of weld pool under different welding speed (a) 1 m/min (b) 2 m/min (c) 3 m/min (d) 5m/min.....	21
Figure 2.6. Image segmentation for processing.....	22
Figure 2.7. (a) Original color image (b) Transformed grey image.....	22
Figure 2.8. Flowchart of boundary extraction.....	23
Figure 2.9. (a) Non-edge point (b) Edge point.....	24
Figure 2.10. (a) Extracted keyhole area by binarization (b) Extracted keyhole boundary (c) Central line and keyhole boundary.....	25
Figure 2.11. Histogram and image before (top) and after (bottom) the using histogram equalizer.....	26
Figure 2.12. Pixel greyness of the start line.....	27
Figure 2.13. Searched left and right boundary point.....	29

Figure	Page
Figure 2.14. Coordinate of captured image and searching direction in different part.....	29
Figure 2.15. Extracted tail part boundary.....	31
Figure 2.16. First point search on central line.....	32
Figure 2.17. Extracted head part and tail part boundary.....	33
Figure 2.18. Entire boundary of weld pool.....	34
Figure 2.19. Real weld seam and corresponding extracted weld pool geometry.....	36
Figure 2.20. Calculated weld pool width.....	37
Figure 2.21. Top view of welding seam.....	38
Figure 2.22. Cross-section view of weld pool.....	38
Figure 2.23. Combined view of monitored weld pool and modeling result for stainless steel.....	41
Figure 2.24. Boundary extraction for magnesium alloys AZ31B (800W, 2 m/min).....	42
Figure 2.25. Boundary extraction for magnesium alloys AZ31B (900W, 2 m/min).....	42
Figure 2.26. Combined view of monitored weld pool and simulation result for magnesium alloys (900W, 2 m/min).....	43
Figure 2.27. Extracted boundary of other cases.....	44
Figure 3.1. Schematic diagram of RBFNN.....	46
Figure 3.2. Static radial basis function neural network for keyhole dynamics.....	48
Figure 3.3. Dynamic radial basis function neural network model for keyhole dynamics....	49
Figure 3.4. Structure of estimator based on RBFNN.....	53
Figure 3.5. Detected keyhole area and keyhole diameter.....	54
Figure 3.6. Keyhole diameters under different welding parameters.....	54
Figure 3.7. Cross section view to for penetration depth measurement (800 W, 2m/min)...	56
Figure 3.8. Cross-section view for keyhole inclination angle (Left: 1000 W, 1 m/min. Right: 1000 W, 2 m/min).....	57
Figure 3.9. Experimental data for penetration depth (left) and inclination angle (right)...	57
Figure 3.10. Training results and errors of penetration depth.....	58
Figure 3.11. Training results and errors of inclination angle.....	59

Figure	Page
Figure 3.12(a). Penetration depth of (a) 500 W, 2 m/min (b) 500 W, 3 m/min (c) 500 W, 4 m/min.....	60
Figure 3.12(b). Inclination angle of (a) 500 W, 2 m/min (b) 500 W, 4 m/min.....	60
Figure 3.13. Training data from numerical simulations (Case of changing power).....	61
Figure 3.14(a). Dynamic neural network training results for changing laser power.....	62
Figure 3.14(b). Dynamic neural network training results for changing welding speed.....	62
Figure 3.15. Comparison of estimated penetration depth and experimental results for (a) changing power (b) changing speed.....	64
Figure 3.16. Comparison of numerical model-based actual angle and estimated angle (a) Changing power (b) Changing speed.....	65
Figure 3.17. Keyhole area detection with stainless steel (a) Original image (b) Converted grey image (c) Binarized image.....	66
Figure 3.18. Keyhole area detection with magnesium alloy (a) Original image (b) Converted grey image (c) Binarized image.....	67
Figure 3.19. Horizontal cross section view of weld on stainless steel.....	69
Figure 3.20. Longitudinal cross section view of weld on magnesium.....	69
Figure 3.21. Detected keyhole sizes with stainless steel.....	71
Figure 3.22. Detected keyhole sizes with magnesium alloys.....	72

## ABSTRACT

Luo, Masiyang. M.S.E., Purdue University, August 2014. Weld Pool and Keyhole Dynamic Analysis Based on Visual System and Neural Network during Laser Keyhole Welding. Major Professor: Yung Shin, School of Mechanical Engineering.

In keyhole fiber laser welding processes, the weld pool behavior and keyhole dynamics are essential to determining welding quality. To observe and control the welding process, the accurate extraction of the weld pool boundary as well as the width is required. In addition, because of the cause-and-effect relationship between the welding defects and stability of the keyhole, which is primarily determined by keyhole geometry during the welding process, the stability of keyhole needs to be considered as well.

The first part of this thesis presents a weld pool edge detection technique based on an off axial green illumination laser and a coaxial image capturing system that consists of a CMOS camera and optic filters. According to the difference of image quality, a complete developed edge detection algorithm is proposed based on the local maximum gradient of greyness searching approach and linear interpolation. The extracted weld pool geometry and the width are validated by the actual welding width measurement and predictions by a numerical multi-phase model.

As for the keyhole dynamics, three essential attributes to describe the simplified three-dimensional keyhole shape include keyhole size, penetration depth and keyhole

inclination angle. However, when using traditional measurement techniques, it is very challenging to take in-process measurements of penetration depth and inclination angle, even if the keyhole size can be detected by using a visual monitoring system. To realize the on-line estimation of keyhole dynamics and welding defects, a data-based radial basis function neural network state observer is adopted for estimating penetration depth and inclination angle in the transient state when welding parameters change suddenly. First, a static neural network is trained in advance to establish a correlation between the welding parameters and unobservable keyhole geometry. The dynamic state observer is trained based on the transient welding conditions predicted by a numerical model and then used to estimate the time-varying keyhole geometry. Meanwhile, the coaxial monitoring system is used to observe the keyhole shape from the top side in real time, which not only provides input to the neural network but also indicates the potential welding porosities. The predicted results are validated by experimental data performed by welding with stainless steel 304 and magnesium alloy AZ31B.

## CHAPTER 1. INTRODUCTION

### 1.1 Motivation and Literature Review

#### 1.1.1 Keyhole Laser Welding

Laser welding has been a promising welding technique in industrial manufacturing owing to its high density energy, low heat input, large depth-to-width ratio, small heat-affected zone (HAZ), and high speed [1]. All laser welding techniques can be classified into two basic categories: keyhole or conduction welding. Keyhole, or deep penetration welding, is probably the most popular welding form.

In keyhole welding, the laser beam is focused on a small spot to obtain a high power density at the surface of a workpiece. The temperature of the fusion zone is rapidly elevated to the evaporating point where a vapor cavity, known as a keyhole, is formed due to the influence from recoil pressures, vapor plume impacts and other forces. Vapor pressure holds back the surrounding molten metal and keeps this hole open during the process. The metal vapor also scatters the laser beam into the molten metal along the side of the keyhole, thus transferring energy through the entire depth of the keyhole, resulting in a weld with a high aspect ratio, as illustrated in Figure 1.1.

The small size of the keyhole region results in relatively small zones for both the fusion zone and the heat-affected zone. Furthermore, the highly localized application of heat means that the workpiece both heats up and cools down rapidly, which can minimize

grain growth in materials. Even though no filler material is typically used for keyhole welding, the high temperatures of keyhole welding can vaporize the materials and produce a different composition in the fusion zone than in the base metal.

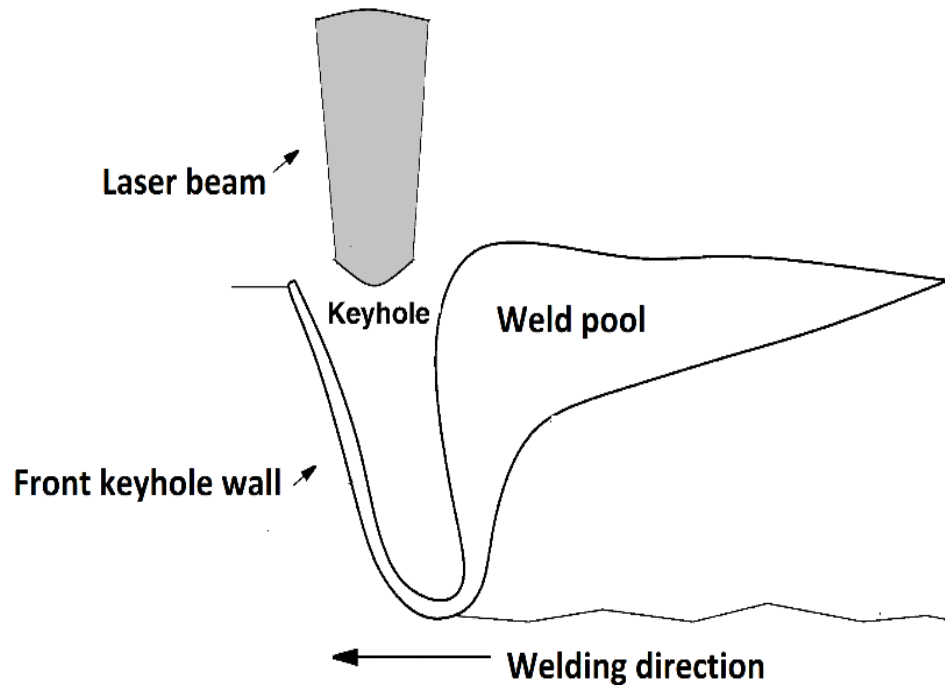


Figure 1.1. Schematic of keyhole welding.

### 1.1.2 Numerical Model Simulation of Laser Welding

While keyhole welding has been given much attention and extensive study, the instability of the keyhole and the weld pool still generate some defects during the welding process. Hence, to ascertain the keyhole and weld pool dynamics, especially their shapes during deep penetration welding, much research has been conducted on the modeling of keyhole and weld pool changes in terms of different physical assumptions.

Matsunawa and Semak [2] developed a simulation model of the front keyhole wall behaviour on the basis of a hydrodynamic model that assumed that only the front

part of the keyhole wall is exposed to the high-intensity laser beam and the growth of the keyhole wall inside the material is due to melt expulsion. The front keyhole wall profile distribution of absorbed laser intensity and phase velocity of the solid and liquid boundary were calculated for different processing parameters, which showed that depending on the processing conditions, the absolute value of the keyhole wall velocity component parallel to the translation velocity vector can be higher than, smaller than, or equal to the beam translation speed.

To obtain a better understanding of the keyhole geometry, Lankalapalli et al. [3] developed a model for estimating penetration depth based on a two-dimensional heat conduction model and a conical keyhole assumption. Later, he proposed another modified model-based approach [4] for laser weld penetration monitoring, instead of a purely empirical correlation between a measured signal (acoustic, infrared, etc) and the penetration depth to estimate the welding depth for bead-on-plate welds on low-carbon steel plates. On the other hand, Ye et al. [5] assumed a cylindrical keyhole and studied the effects of welding speed, Marangoni force, and natural convection on melt flow and heat transfer. A method was outlined to use the three-dimensional modeling results to estimate the keyhole radius or predict the energy efficiency in the laser full-penetration welding.

However, these simplified models may not be able to accurately reflect the real dynamic changes of the keyhole; thus, numerical modeling work has been conducted to develop more complex models which describe these changes. Ronda et al. [6] investigated the relationship between the shape of the keyhole, surface tension and a recoil force based on numerical simulation. This model of keyhole formation took into



consideration the temperature dependence of material parameters and characteristics of a laser beam, as well as considering the influence of the sulphur content on surface tension. Ki et al. [7,8] developed more complicated and well-considered models based on level-set equations. The model featured the self-consistent evolution of the liquid/vapor (L/V) interface together with full simulation of fluid flow and heat transfer. Important interfacial phenomena, such as free surface evolution, evaporation, and multiple reflections were applied in the model. In addition, Pang et al. [9] proposed a three-dimensional sharp interface model, which combined three-dimensional heat transfer, keyhole free surface evolutions, and fluid flow in the welding process. In this model, not only the keyhole wall but also periodical keyhole collapse and bubble formation processes could be simulated successfully. Another model considering plasma gas, liquid metal and solid metal was proposed to describe the keyhole phenomena of laser welding by Zhao et al. [10]. In their work, the forces of interaction of fluid dynamics in the keyhole and molten pool were modeled and an adaptive heat source model was proposed for the absorption of laser energy.

More recently, based on the study of all the previous models, Tan et al. [11] used a multi-phase numerical simulation combining the level-set model and a sharp interface model to accurately capture the dynamics of the keyhole, the molten pool and even the plume. The model revealed that plume attenuation due to the particle absorption and scattering could be significant in fibre or Nd :YAG laser-based keyhole welding. Moreover, the temperature on the keyhole wall was accurately calculated. This model has been validated against multiple experiments with both stainless steel and magnesium alloys.

### 1.1.3 Weld Pool Monitoring

To fully understand dynamic keyhole welding and improve the weldment quality, a variety of research has been carried out in addition to the development of numerical models, such as the assisted shield gas application [12-14] and weld pool monitoring [15-25]. Since the weld pool contains useful information related to welding quality, on-line weld pool monitoring techniques have been developed over the past decade.

Li et al. [15] used the “acoustic mirror” to study the ultrasonic airborne acoustic emission of weld pool plasma and laser beam. The characteristics of two types of ultrasonic acoustic emissions observed in laser material processing involving melting, vaporization and plasma generation were compared. Wang et al. [16] and Huang et al. [17] measured welding temperature distributions by an IR thermography system, which was calibrated by thermocouples.

At present, as a result of the continuous development of visual imaging techniques and high computational capability with a reduction of cost, a vision-based system has become a popular approach to monitoring the weld pool. Captured imaging signals are capable of providing more straightforward welding details, such as variations in weld pool geometry. Measurements have been conducted using a high speed camera and a dot matrix pattern laser so as to reconstruct the three-dimensional weld pool surface in gas tungsten arc welding (GTAW) [18–20]. Among these studies, Kovacevic et al. [20] first defined the weld pool boundary point as the point with a maximum gradient value so as to distinguish the weld pool boundary against the imaging backgrounds. Moreover, a calibrated camera with structured lights was used to directly measure the weld pool depth

in GTAW [21]. However, even if the structured light method has potential to detect the three-dimensional shape of the weld pool, it is limited to the GTAW since the weld pool is not very deep compared with keyhole laser welding. In keyhole welding, the structured light could hardly be reflected from the keyhole area.

In order to capture the two-dimensional geometry of the weld pool in keyhole welding, a coaxial monitoring system was developed. With this type of system, which consisted of a coaxial image camera and a coaxial illumination laser, Kim et al. [22] investigated the size of the keyhole area by testing various optic filter combinations with a coaxial illumination laser under different welding conditions. However, the setup of the coaxial illumination laser made the entire monitoring system, as shown in Figure 1.2, too complicated to be used in a wider range of situations. Qin et al. [23] extracted molten pool edges by taking advantage of the binarization algorithm. However, these methods were too simple to capture the dynamic details of the weld pool.

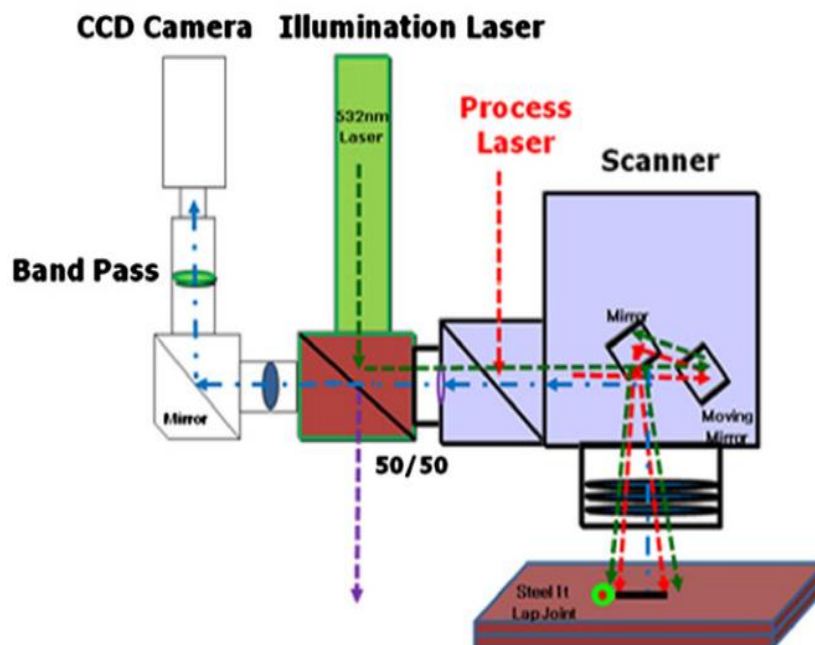


Figure 1.2. Coaxial monitoring system with coaxial illumination [22].

Recently, Zhang et al. [24] built an on-line coaxial monitoring system with an auxiliary illuminant for the fiber laser welding of Zn-coated steel and proposed a region-growing method with the Canny algorithm to extract the boundary of the weld pool. The extracted result is shown as Figure 1.3. Even though their algorithm was computationally efficient and accurate, their image processing method may not be able to deal with other materials—such as magnesium alloys—which produce low-quality images with more welding noise. In terms of weld pool reflection features, a more complex edge detection algorithm was designed on the edge enhancement [25]. However, the lack of illumination made a slow transient region occur between the image background and the weld pool area, which introduced some uncertainties into the weld pool edge detection.

Additionally, the lack of comparison between the actual welding width and the monitored one also brings up the unknown reliability of the image processing results.

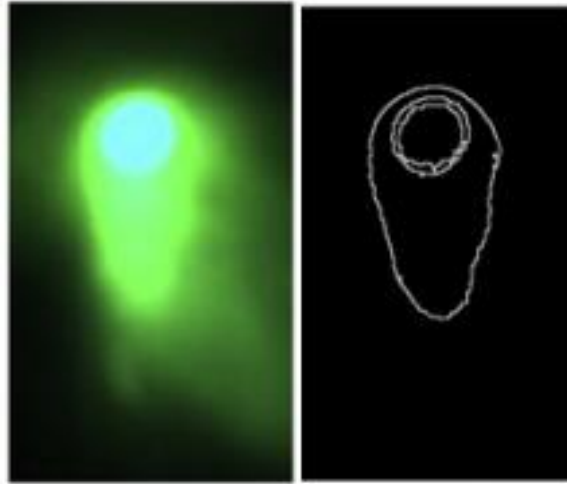


Figure 1.3. Captured weld pool image and extracted weld pool boundary [20].

#### 1.1.4 Observation of Keyhole Dynamics

Although various numerical models are capable of describing the transient keyhole shape, they cannot be used for real-time applications due to their high computational requirements. Because of the great amount of data required for keyhole analysis and the associated time and cost, other studies focusing on keyhole dynamics have been carried out through multiple experimental observation techniques.

Among these, a high-speed camera-based vision system has been developed by Fabbro et al. [26-28] to learn the keyhole behavior in full-penetration laser welding. The penetration depth and keyhole front tilting angle were two significant areas of focus in this study, for which the collected data are shown in Figure 1.4. The analysis of this penetration curve on a very large range of welding speeds, typically from 0 to 15 m/min, allowed them to observe very different regimes, which are mainly characterized

according to the physical processes by which they impede the laser beam penetration inside the material. Additionally, the dynamics of the keyhole and its complete geometry, including front wall inclination, and top and bottom apertures, were analyzed for differing experimental condition. The related keyhole dynamic models were also introduced to validate their experimental results.

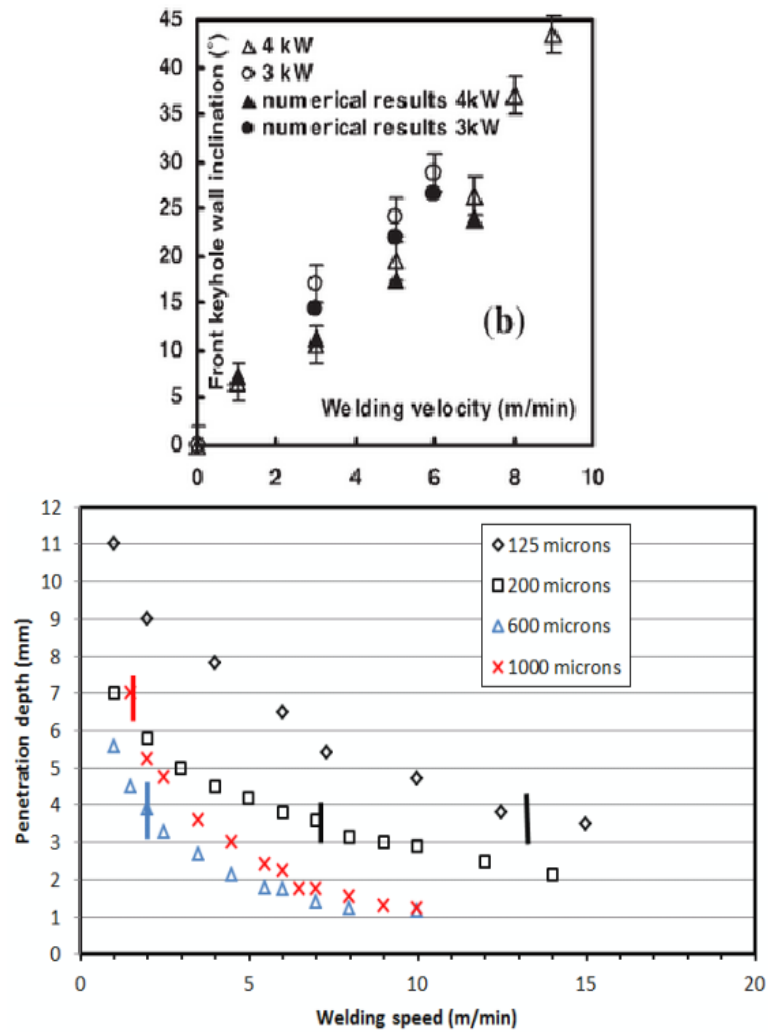


Figure 1.4. Collected data for inclination angle and penetration depth with different welding conditions (for four different focal spot diameters: 125 and 200  $\mu\text{m}$  (4 kW, Nd-Yag laser), 600 and 1000  $\mu\text{m}$  (4 and 6.3kW, diode laser)) [26].

A study at Osaka University incorporated more complicated measurement techniques, utilizing high-speed video cameras and an X-ray transmission real-time imaging system to investigate the dynamic phenomena inside the keyhole and the weld pool with different materials, such as stainless steel and magnesium alloy [29,30]. In the process of deep-penetration laser welding, due to the high energy density of the heat input source on the workpiece, the material evaporates rapidly and the formed keyhole is unstable. As the liquid flow is very complicated and the keyhole geometry fluctuates frequently under some welding conditions, this would influence the quality and performance of the welding joint. For instance, the bubbles formed from keyhole collapse and shrinkage cause keyhole-induced porosity. Based on the X-ray imaging system, the formation of bubbles and welding porosities could also be captured in real time, as shown in Figure 1.5 [29,31-33]. However, the high cost of the whole system and overly complicated imaging signals of the keyhole make this monitoring system unsuitable for implementation as a real welding process control system.

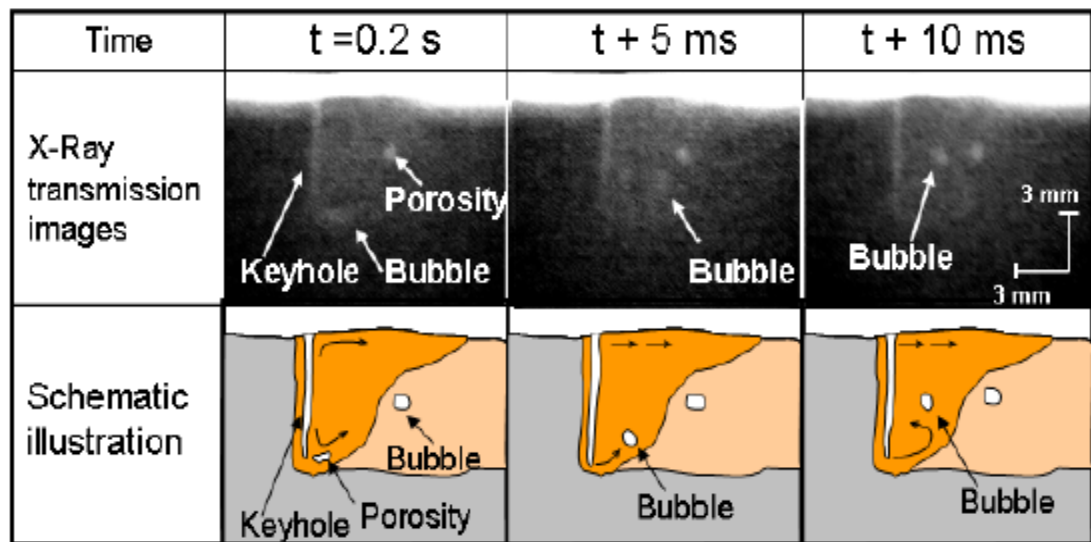


Figure 1.5. Detection of welding porosity and bubble of using X-ray imaging system [29].

### 1.1.5 Neural Network Based System Identification and State Observer Design

Keyhole dynamics is very important in the keyhole welding process because it can directly impact welding quality. However, an accurate mathematical model that could depict the keyhole dynamics is not readily available, and it would be difficult to use for real-time applications. Thus, to learn the keyhole dynamics, some system identification techniques could be considered. Among these, the neural network-based system identification methods are most popular.

Lu et al. [34] studied the problem of identification for nonlinear systems in the presence of unknown driving noise, using both feedforward multilayer neural network and radial basis function network models. Xu et al. [35] developed and implemented neural network-based system identification techniques for nonlinear systems with the specific goal of residual generation for default detection purposes. Two neural network structures were investigated: the partially connected neural network (PCNN) and the conventional fully connected neural network (FCNN). Both methods were tested on a Boeing 747 aircraft model. Ranković and Nikolić [36] studied nonlinear system identification via feedforward neural networks (FNN) and digital recurrent networks (DRN). A dynamic backpropagation algorithm was employed to adapt weights and biases of the DRN. Moreover, fuzzy logic and neuro-fuzzy systems (ANFIS) have also been used in identification of nonlinear dynamics.

In control theory, a state observer provides an estimate of the internal state of a given real system by using measurements of the input and output of the real system. In most practical cases, the physical state of the system cannot be determined by direct



observation. However, indirect effects of the internal state are observed through the system outputs.

For the linear system, Kalman [37] developed a very well-known filter, named the Kalman filter, to operate recursively on a series of noisy input data to produce a statistically optimal estimate of the system state. This theory has been applied to many fields, such as navigation, vehicle control, etc. For nonlinear systems, extended Kalman filter methods [38] were developed relying on linearized state and output equations. The EKF is based on first-order Taylor approximations of state transition and observation equations about the estimated state trajectory. However, the Taylor linearization provides an insufficiently accurate representation in many cases, and significant bias, or even divergence, due to the overly crude approximation. Norgaard et al. [39] proposed a new set of estimators, divided difference filter (DDF), which were based on polynomial approximations of the nonlinear transformations obtained with a particular multidimensional extension of Stirling's interpolation formula. In contrast to Taylor's formula, no derivatives are needed in the interpolation formula. On the basis of the DDF, Subrahmanya and Shin [40] presented a novel adaptive version of the DDF applicable to non-linear systems with a linear output equation. In order to make the filter robust to modeling errors, upper bounds on the state covariance matrix were derived, which made this filter capable of estimating the states in a time-varying system.

However, all the estimation methods introduced above require exact models of underlying nonlinear systems, which are often difficult to obtain in reality and can also lead to divergence when modeling errors exist. Therefore, Elanayar and Shin [41] used a radial basis function neural network (RBFNN) to approximate the unknown nonlinear

system and developed a new state observer based on RBFNN. Since the parameters appeared in the RBFNN as a linear form, least squares estimation was possible. The state estimator was designed for use with the RBFNN and the gain matrix was derived on the basis of an upper bound covariance matrix. In addition, the consideration of approximation error in the estimation algorithm successfully minimized filter divergence. After the development of this observer, Elanayar and Shin [42] used it for tool wear estimation in real time. The dynamic process of flank wear and crater wear with respect to time under different cutting forces and feed rates were identified by RBFNN. The on-line estimation of both types of wear was then conducted successfully based on this well-trained RBFNN and proposed state observer.

## 1.2 Objectives of Thesis

The main objective of the present work, which focuses on weld pool and keyhole dynamic analysis based on visual system and neural network in laser keyhole welding, could be divided into the following parts:

- (1) Design an easily-implementable monitoring system, which could detect the weld pool and keyhole geometry from the top side in real time during a welding process.
- (2) Develop an efficient and accurate weld pool boundary extraction algorithm that aims at dealing with the noise in captured weld pool images.
- (3) Based on experimental data, establish a static neural network model to correlate the welding parameters and system measurements to unobservable keyhole geometric features.

- (4) Based on a well-trained static neural network model, develop a dynamic neural network model which could approximate the keyhole dynamics and use the radial basis function neural network-based state observer [41] to estimate the keyhole dynamics in the transient state of welding.
- (5) Predict the welding defects (bubbles or porosities) by analyzing the captured imaging signals of the keyhole area.

### 1.3 Overview of Thesis

Chapter 2 describes the experimental system with the coaxial monitoring setup and presents the algorithms used for boundary extraction of the weld pool and calculation of the weld pool width. The results are compared with the accurate weld pool width and prediction of numerical simulation [8].

Chapter 3 introduces the methodology of estimating keyhole dynamics, data collection, static neural network and dynamic neural network training results and estimation results of keyhole dynamics under different welding conditions. In addition, this chapter presents the methods of welding defect prediction along with experimental validation with both stainless steel and magnesium alloys.

Chapter 4 presents the conclusion of the current work and the recommendations for future work.

## CHAPTER 2. EXTRACTION OF WELD POOL BOUNDARY

This chapter describes an efficient weld pool boundary extraction algorithm that aims at dealing with the noisy captured weld pool images in keyhole fiber laser welding based on a coaxial monitoring system with the green laser illumination. According to the different noise disturbance level, a searching technique for the local maximum gradient of grayness is developed for detecting clear weld pool edges (in the head and tail parts of the captured images). Although the boundary points can be defined straightforwardly as the ones with the maximum gradient of grayness [14], more well considered image processing procedures and initial point or start line selection methods are used to reduce the effects of noise and to guarantee the rightness of weld pool width calculation. The linear interpolation is adopted to reshape the blurred weld pool boundary (in the middle part). The width of the weld pool is then calculated via the acquired edge data in order to analyze the relationship between the different welding conditions and the corresponding weld pool geometries. Eventually, some unique methods are proposed to validate the image processing results.

### 2.1 Experimental Setup

The keyhole welding is performed by a fiber laser (IPG photonics YLS-1000, details of which are shown in Table 2.1) with a focal diameter of 200  $\mu\text{m}$ . The laser

beam is transmitted through the fiber to the laser head and its wavelength is 1070 nm. The laser details are shown in Table 2.1. The assisted gas Argon is blown into the weld pool to improve the weldment quality in the experiments. The 304 stainless steel with 2 mm of thickness is used as the substrate material. The chemical composition of the 304 stainless steel is listed in Table 2.2. The welding process is controlled by the three-axis Mazak Controller.

Table 2.1. Description of IPG YLS-1000 fiber laser.

<b>Available Output Power</b>	$\leq 1000$ W
<b>Emission Wavelength</b>	1070 nm~1080 nm
<b>Diameter of feed fiber</b>	200 $\mu$ m
<b>Dope material</b>	Ytterbium
<b>Wall-plug efficiency</b>	$> 30\%$

Table 2.2. Chemical composition of stainless steel 304.

<b>Element</b>	C	Mn	P	S	Si	Cr	Ni	N	Fe
<b>Portion(%)</b>	0.08	2	0.045	0.03	0.75	10	10	0.1	balance

To observe the keyhole from the topside, a coaxial vision-based monitoring system was designed. The coaxial monitoring system is composed of two dichroic mirrors, a complementary metal-oxide-semiconductor (CMOS) camera (DFK 42BUC03), and an illumination resource and optic filters. The entire monitoring system and the laser head are all mounted on the Mazak CNC machine, as illustrated in Figure 2.1. Two dichroic mirrors are set parallel to each other into a parallelogram block so that the output beam can be perfectly focused on the base material, as schematically shown in Figure 2.2. The

pre-set resolution of the camera is 1280x720 pixels with a maximum frame speed of 33 frames/s.

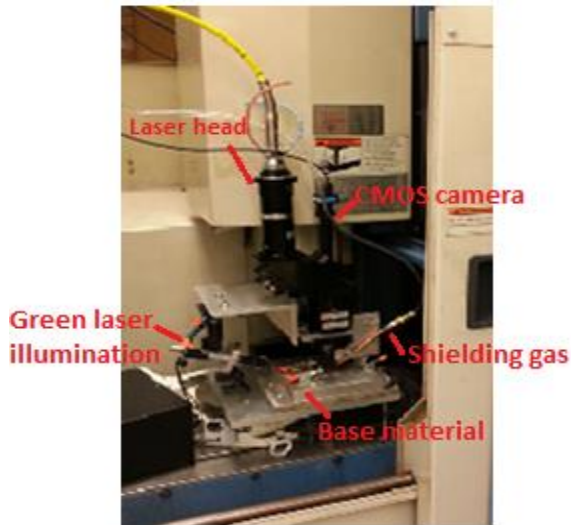


Figure 2.1. Photo of coaxial monitoring system and Mazak Controller.

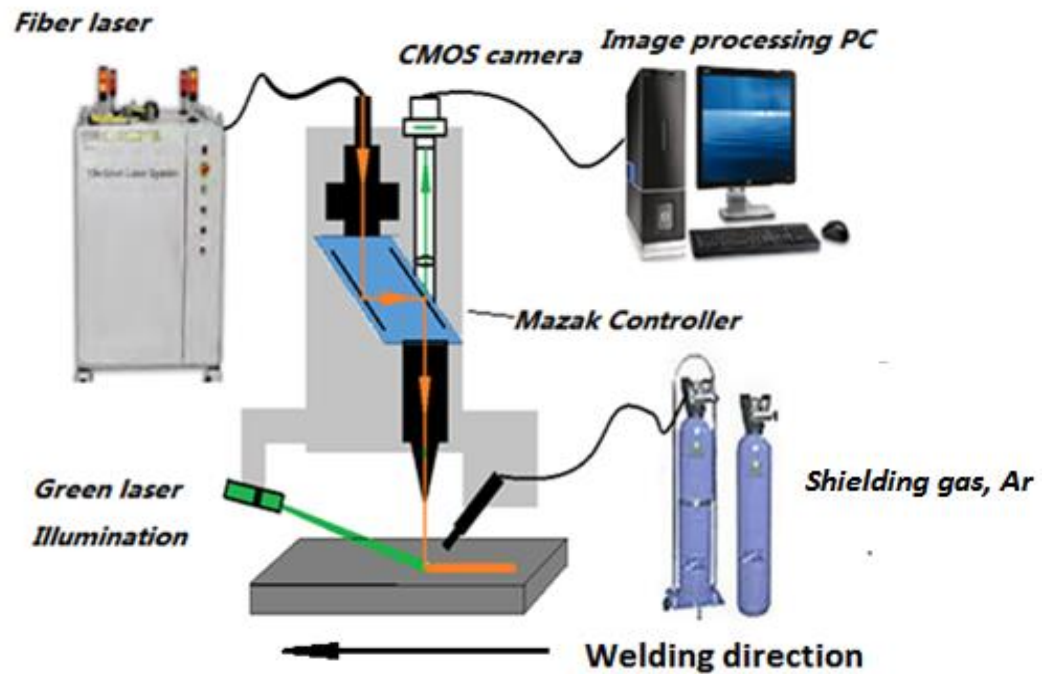


Figure 2.2. Coaxial visual monitoring system.

In the keyhole welding, the irradiation object is not only the light emission of weld pool, but also ionized metal plasma, which is much weaker though. To get a better understanding of the spectra of disturbing irradiations, a spectrometer is mounted horizontally above the workpiece to gather the wavelength distribution of the welding plasma prior to the actual weld pool measurement. The average result attained from the multiple experiments is shown in Figure 2.4. It is apparent that the wavelength from 550 nm to 650 nm (ionized iron) is the strongest portion, which is consistent with the Table 2.2. The sharp peak at around 1070 nm happens due to the reflected laser beam.

According to the collected data by the spectrometer, the green light with the low plasma interference and the high camera sensitivity response is chosen as illumination resource to capture the clear image of the weld pool. A 200 mW focus-adaptable green laser with the wavelength close to 530 nm was chosen as the illuminant. The illuminating area is adjusted to cover the entire weld pool region. Simultaneously, a narrow band pass filter with the center wavelength of 532nm and a ND16 filter were coupled together in front of the CMOS camera to enhance the illuminated weld pool features.

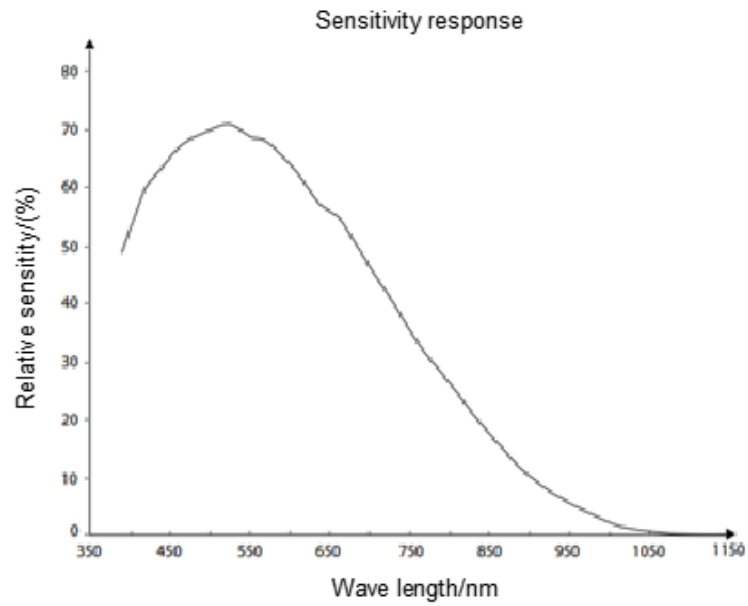


Figure 2.3. Relative sensitivity response of CMOS camera used.

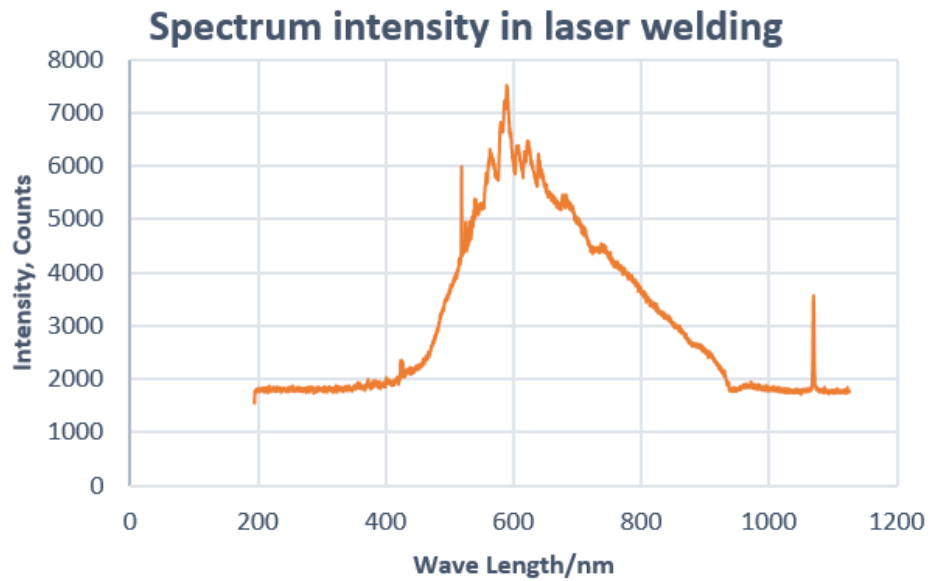


Figure 2.4. Plasma spectrum in keyhole welding.



## 2.2 Boundary Extraction and Width Measurement

In the welding experiments, the coaxial weld pool monitoring consists of video recording and on-line image processing. The images of the monitored welding process are recorded in 'AVI' format and then each frame is processed to extract weld pool boundary, followed by the calculation of the welding width. The experimental welding speed ranges from 1 m/min to 5 m/min. Figure 2.5 shows the original unprocessed images with varied welding speeds. The welding power is maintained at 1 kW for all the experiments. Although the green laser illumination helps increase the contrast level of weld pool boundary, from the images shown in Figure 2.5 (b), much of imaging noises are mostly induced by both undesired illumination reflection and the imaging capability of the camera, such as the limited frame-per-second (FPS). Intuitively, the weld pool becomes narrow as the welding speed increases. However, to measure the exact variations of weld pool geometry, further steps are made as described in following sections.

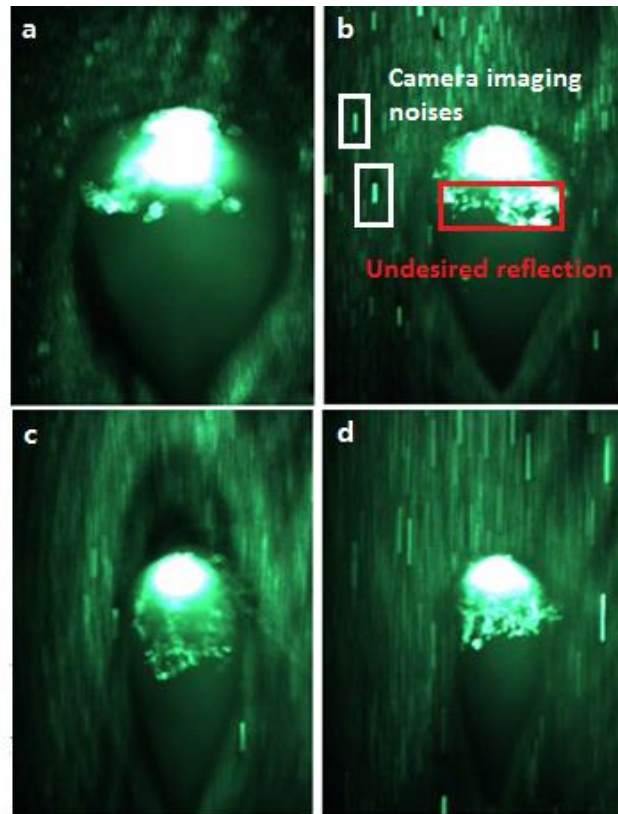


Figure 2.5. Original images of weld pool under different welding speed (a) 1 m/min (b) 2 m/min (c) 3 m/min (d) 5m/min.

### 2.2.1 Analysis of image signal

According to the characteristics of the weld pool images, the edge detection process is classified into three groups: the head, the middle and the tail part, as shown in Figure 2.6. In the head part, the existence of keyhole increases the overall brightness nearby so that the region inside the head part of weld pool is much brighter than the other areas. In the tail part, however, the difference between the weld pool and the imaging background (non-melt material) is not that distinctive, but the weld pool profile and the heat affected zone (HAZ) [14] are separated by the slim dark gap. Between the head part and the tail part, there is a relatively narrow but special region, the middle part, where the

imaging noises of isolated arbitrary bright spots make the edge of the weld pool difficult to locate.

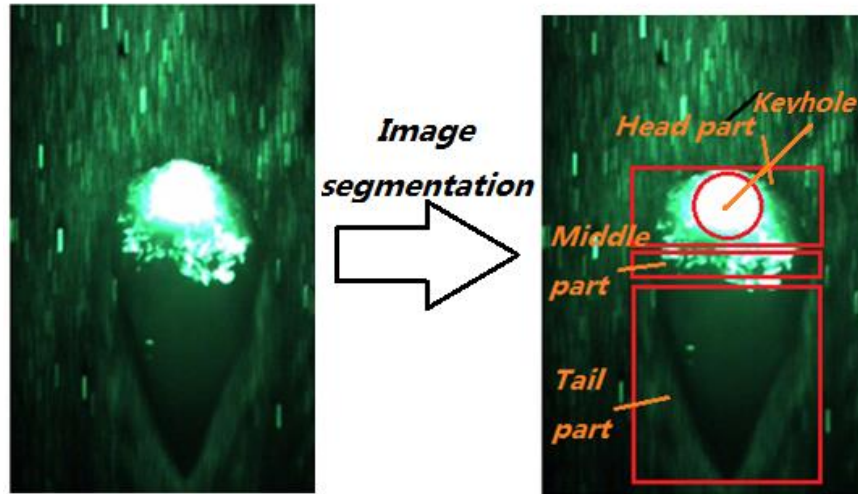


Figure 2.6. Image segmentation for processing.

Regarding the green light illumination, only the green primary component of the original color images is processed in this study to improve the image processing speed. The transformed gray image based on the green primary color is shown as Figure 2.7. The proposed boundary extraction procedure is schematically shown in Figure 2.8.

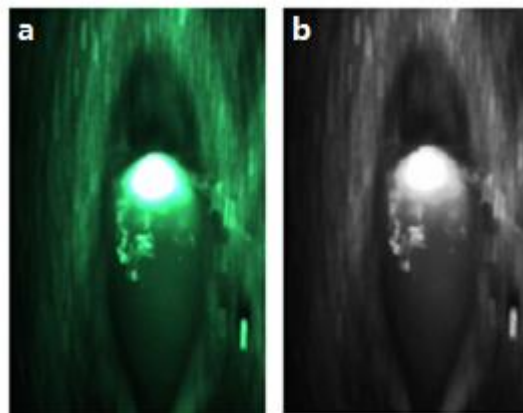


Figure 2.7. (a) Original color image (b) Transformed grey image.

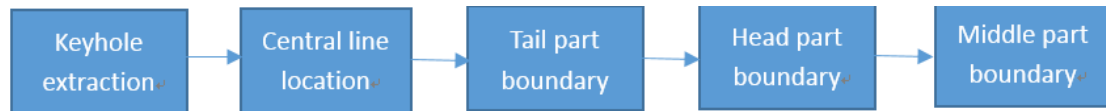


Figure 2.8. Flowchart of boundary extraction.

### 2.2.2 Keyhole Extraction and Central Line Location

For the transformed image, each pixel has a grey level value between 0 and 255. The algorithm proposed for extracting the keyhole area is based on the binarization with a high threshold value in terms of the extreme bright feature of the keyhole. In this work, the threshold is defined as 245 according to the image feature that the greyness value of the keyhole area is close to saturation. Any pixels with a value greater than this threshold are set to 255 in grey level, otherwise 0. Due to the symmetry of the weld pool image, a symmetric central line (SCL) of the weld pool is calculated for the convenience of searching candidate edge points in the following sections. The calculation of SCL is conducted through the extracted keyhole boundary in this part. Since the relative positions of the weld pool in all captured images are fixed, the SCL only needs to be obtained once in the real experiments. The keyhole edge detection and the SCL calculation algorithm are described in the following.

- (1) Boundary point is defined as the point with grey level value 255, but at least one of all the other 8 pixels around is 0, as illustrated in Figure 2.9.

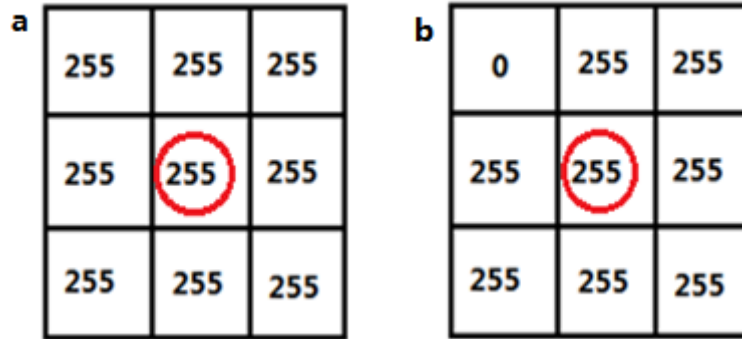


Figure 2.9. (a) Non-edge point (b) Edge point.

- (2) Scan all pixels in the binarized image and use the criterion of (1) to mark all the boundary points.
- (3) After attaining all the boundary points, as shown in Figure 2.10 (b), calculate the distance between the most left point  $P_l^i$  and the most right point  $P_r^i$  in each row  $i$  as  $L_i = P_r^i - P_l^i$ , where  $0 < i < m$ , and  $m$  is number of rows. The distance  $L$  represents the number of pixels between these two edge points. Find the row  $i_{max}$ , which has the largest value of  $L$ , which indicates the widest part of the keyhole area. The coordinate position of the center point in this row is  $P(i_{max}, (P_r^i + P_l^i)/2)$ . Then the central symmetric line can be described as a vertical line which goes through the point P. Figure 2.10 shows the extracted keyhole boundary and the calculated SCL.

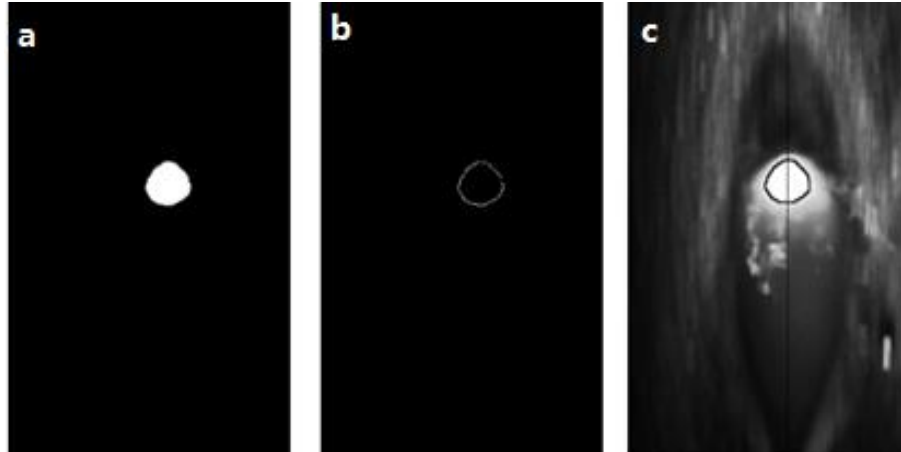


Figure 2.10. (a) Extracted keyhole area by binarization (b) Extracted keyhole boundary (c) Central line and keyhole boundary.

### 2.2.3 Weld Pool Boundary Extraction for Tail Part

From the grey level image, even though the boundary of weld pool in the tail part might be clear to human's vision, it is still not clearly distinguishable for the machine vision. Some improvements of the image quality need to be made In advance. In this work, the histogram equalizer is used to increase the contrast of the image. This method usually increases the global contrast of the image, especially when the usable data of the image is represented by close contrast values, such as the case of the weld pool edge here. Through this adjustment, the intensities can be better distributed on the histogram. This allows for the weld pool areas of lower local contrast to gain a higher contrast, as shown in Figure 2.11.

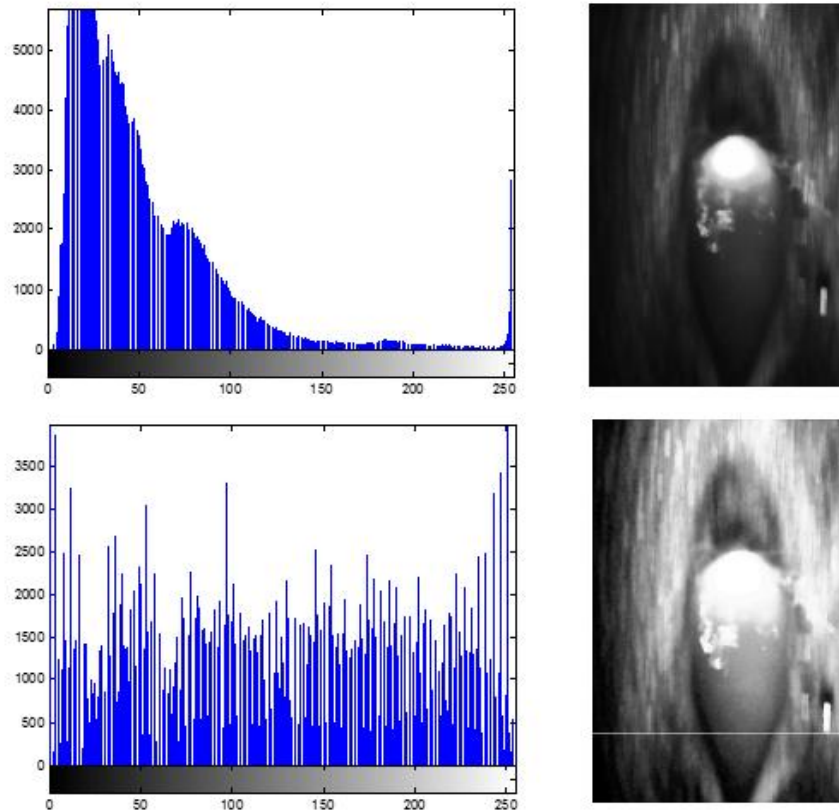


Figure 2.11. Histogram and image before (top) and after (bottom) using the histogram equalizer.

- (1) **Start line:** Pick up one row in the tail part as start line. This line should be chosen between the middle part and the bottom part of the image because of the edge in this area is relatively easy for detecting. In the actual processing, the bottom 130<sup>th</sup> row is picked, shown as the white line in the second image of Figure 2.11.
- (2) **First edge point:** As mentioned earlier the dark area separates the background and weld pool area, so the inner border of the dark area is regarded as weld pool boundary, as shown in Figure 2.12, which has a higher gradient of greyness. To seek the boundary, define the gradient of greyness along -X direction as  $G_L$  and the one along +X direction as  $G_R$ , then  $G_L = G(x, y + \sigma) - G(x, y - \sigma)$  and  $G_R =$

$G(x, y - \sigma) - G(x, y + \sigma)$ , where  $G(\cdot)$  represents the value of greyness, and  $\sigma$  is specified as the step length of greyness, usually 1 or 2. For the first edge point searching,  $x$  is set as the row number of the start line. From the central line to the left side, the maximum value of  $GL$  in the range of 120 pixels is determined as the left edge point. Similarly, from the central line to the right side, the maximum value of  $GR$  in the range of 120 pixels is the right edge point, as shown in Figure 2.13.

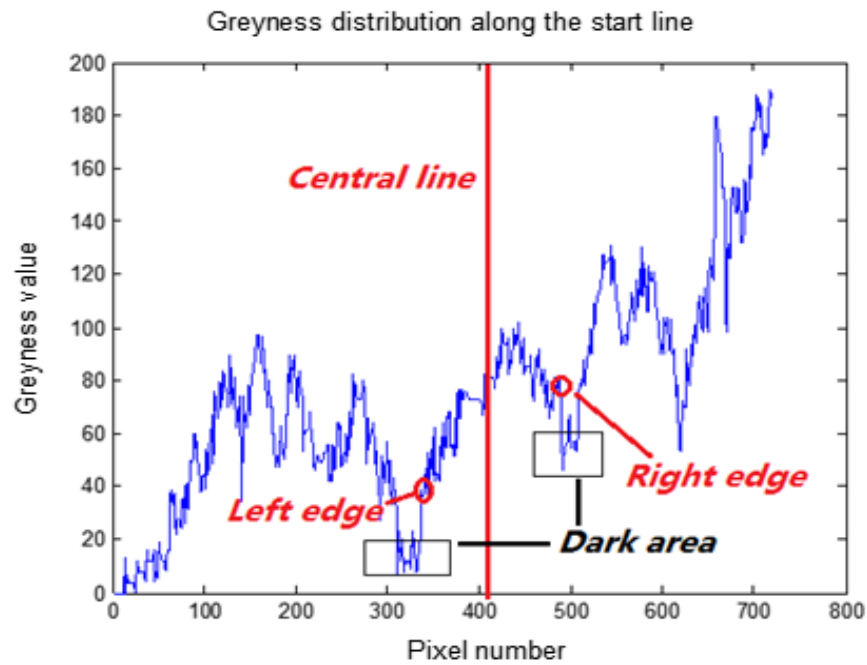


Figure 2.12. Pixel greyness of the start line.



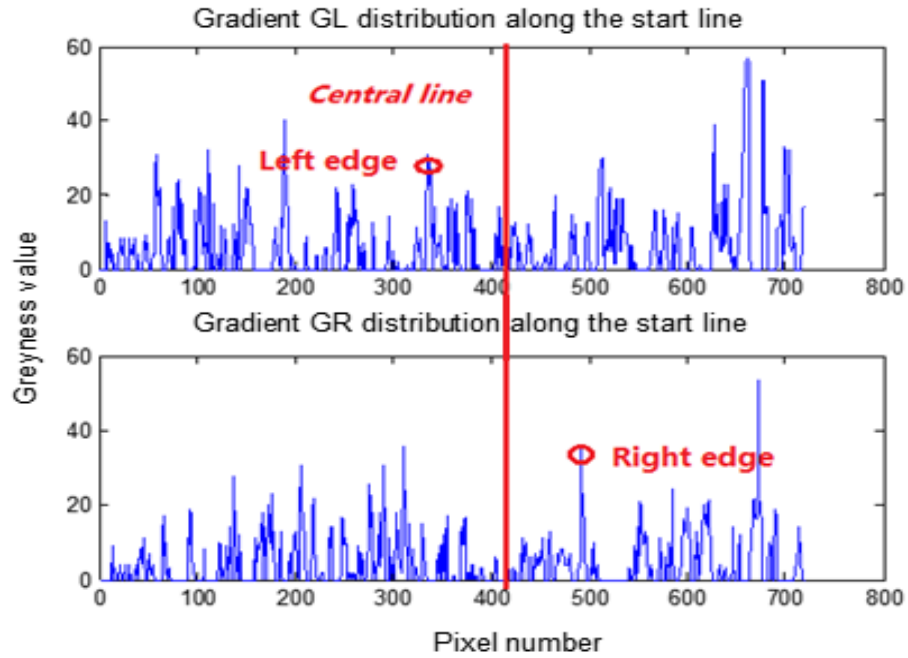


Figure 2.13. Searched left and right boundary point.

- (3) **Tail part boundary extraction algorithm (Local maximum gradient of greyness searching method):** The local maximum gradient of grayness searching algorithm is used to find the new boundary point, which is defined as the one with the maximum gradient of greyness in a certain range determined by the position of current searched boundary point. Assume the first left edge point is  $P_l = (x_l, y_l)$  and the first right edge point is  $P_r = (x_r, y_r)$ . The imaging coordinate and the searching direction are depicted in Figure 2.14. The next searched boundary point of the left side is defined by  $P_{l+1} = (x_{l+1}, y_{l+1})$  while the one of the right side is defined by  $P_{r+1} = (x_{r+1}, y_{r+1})$ .

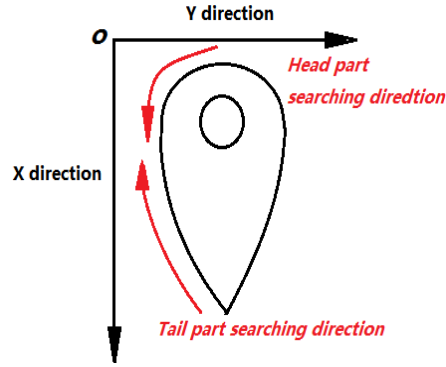


Figure 2.14. Coordinate of captured image and searching direction in different part.

For the left side,

$$\begin{aligned}
 x_{l+1} &= x_l - 1 \\
 y_{l+1} &= \max_{\lambda \in [-\theta_1, \theta_2]} GL(x_{l+1}, y_l + \lambda) \\
 GL(P_{l+1}) &> T \\
 x_l &= x_{l+1} \\
 y_l &= y_{l+1} \\
 &\text{searching continues.}
 \end{aligned}$$

$GL$  has been defined in the **first edge point** of step (2). However, since the weld pool boundary becomes less clear along the searching direction,  $\sigma$  here is selected as a larger number, i.e. 4, so that the gradient values for candidates of the boundary point could still remain distinguishable. Two positive numbers of  $\theta_1$  and  $\theta_2$  determine the searching range. In terms of the blurred boundary, the searching ranges for both the left and right sides are not perfectly symmetric. For the left side,  $\theta_1 > \theta_2$ . Thus, the new boundary points are much more likely to be located to the left side of the previous ones, which is the same as the expectation of actual weld pool boundary profile. When the boundary searching moves to the middle part, the dark area disappears gradually due to the

influence of the keyhole, and the gradient of greyness becomes too small to discern the weld pool boundary. Therefore, a threshold value  $T$  is introduced as a permission of the boundary searching process. If the gradient of the candidate boundary point is less than  $T$ , the tail part searching of the left side ceases.

For the right side, algorithm is similar to the left except that the gradient  $GL$  is replaced by  $GR$  and  $\theta_1 < \theta_2$ .

$$\begin{aligned}
 x_{r+1} &= x_r - 1 \\
 y_{r+1} &= \max_{\lambda \in [-\theta_1, \theta_2]} GR(x_{r+1}, y_r + \lambda) \\
 GR(P_{r+1}) &> T \\
 x_r &= x_{r+1} \\
 y_r &= y_{r+1} \\
 &\textit{searching continues.}
 \end{aligned}$$

The extracted boundary of the tail part is shown in Figure 2.15. For the part below the start line, the same algorithm could also be used except that the searching direction and the relationship between  $\theta_1$  and  $\theta_2$  are changed. For the instance of searching downwards for the left side,  $\theta_1 < \theta_2$ . Similarly,  $\theta_1 > \theta_2$  for the right side. The searching will not stop until the searched boundary point gets to the SCL. The entire processing result is shown as Figure 2.15 (c). It is notable that the most interesting feature of the weld pool is its width in this work, which could be used to not only evaluate the welding process but also validate the extracted weld pool geometry. However, the region below the start line is obviously too narrow to influence the analysis of weld pool width. Thus, to boost the image processing efficiency, the edge searching doesn't have to proceed downwards from the start line in actual experiments.

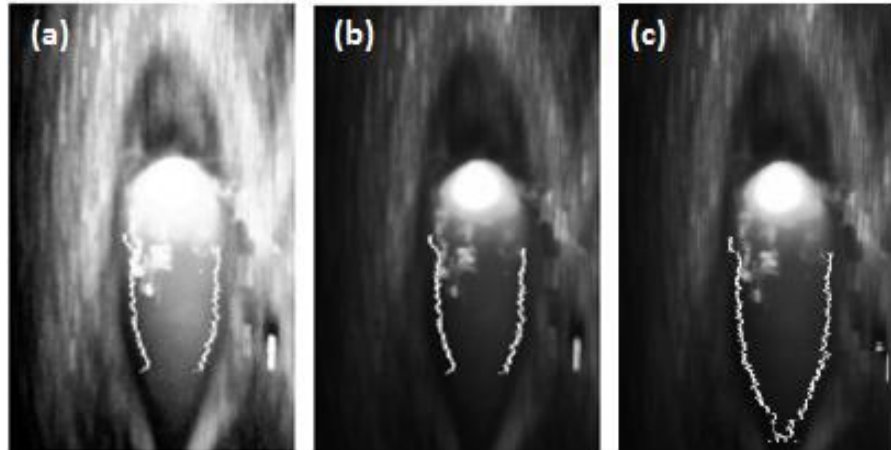


Figure 2.15. Extracted tail part boundary.

#### 2.2.4 Weld Pool Boundary Extraction for Head Part

In the search of the head part edge, the original grey scale image without utilizing the histogram equalizer has a more clear and detailed boundary information. So the non-equalized image is used for the edge detection in the head part. The boundary searching method is similar to the tail part one, which is also divided into the left part and the right part.

(1) **Start point:** Searching downwards along the central line (SCL), find the first point with the grey value larger than 230. Record its position as  $(x_c, y_{cl})$ , as shown in Figure 2.16. In order to remove the influence of the bright isolated dots on the central line, repeat the searching method along the two lines that are 10 pixels away from the central line on the left side and right side. The searched first points are marked as  $(x_{cl}, y_{cl} - 10)$  and  $(x_{cr}, y_{cl} + 10)$ . If  $|x_{cl} - x_c| < 25$  or  $|x_{cr} - x_c| < 25$ , then point  $(x_c, y_{cl})$  is decided to be the start point of the head part. Otherwise, test the second point with the grey value larger than 230 along the central line until an appropriate start

point is found.

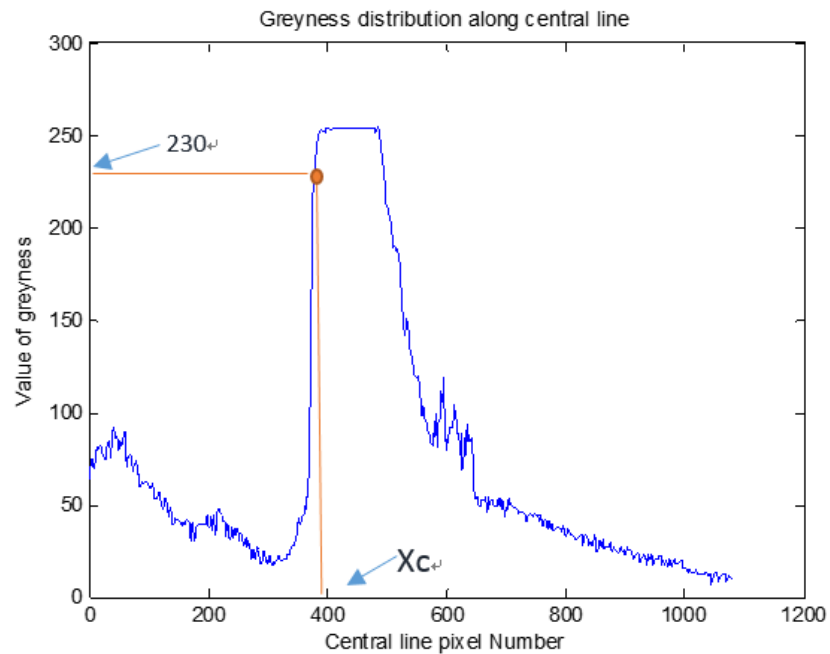


Figure 2.16. First point search on central line.

- (2) **Head part boundary extraction algorithm (Local maximum gradient of greyness searching method):** The same algorithm based on the local maximum gradient of greyness is also applicable in terms of the same boundary feature in both the head and tail part. The searching direction is shown in Figure 2.14. However, the head part searching has to stop when it reaches the middle part where the image quality is lowest due to the transitional region between the extremely bright keyhole area and the relatively dark tail part of weld pool. The result of extracted boundary in the head part is shown as Figure 2.17.



Figure 2.17. Extracted head part and tail part boundary.

#### 2.2.5 Weld Pool Boundary Extraction for Middle Part

In the experiment, the middle part is regarded as the searching gap between the head part and the tail part. Usually, the middle part ranges from 30 pixels to 50 pixels. In this part, besides the transitional region of the bright and the dark, the non-vaporized metal materials (spatters) as well as the plume also strongly reflect the green illumination. These undesired imaging signals generate the arbitrary bright shapes and isolated bright dots (regarded as imaging noises) that increase the difficulty of locating the correct weld pool profile in this part. Therefore, the direct implementation of the proposed searching algorithm could probably generate the serious consequence, even leading to a failure of the calculation for weld pool width.

However, considering the small area of the middle part and the continuity of the weld pool profile, the linear interpolation method is adopted to approximate the actual weld pool boundary. The last searching edge point in the head part and the last searching edge point in the tail part on both the left and right side are connected

through linear interpolation. The interpolated weld pool boundary is eventually shown in Figure 2.18.



Figure 2.18. Entire boundary of weld pool.

#### 2.2.6 Weld Pool Width Measurement

From the extracted boundary, the width of weld pool is defined as the widest distance between the right edge and the left edge. Hence, the width of weld pool can be calculated by the following expression:

$$\text{Width} = \max_{I \in [1, m]} (y_{RI} - y_{LI}),$$

where  $m$  is the total number of rows in the captured images,  $y_{RI}$  is the  $y$  position of the right edge point on the  $I^{th}$  row, and  $y_{LI}$  is the  $y$  position of the left edge point in the  $I^{th}$  row. Finally, to calculate the actual width of the weld pool, the imaging scaling is indispensable. In this hardware set-up, the length of 230 pixels of the image is 1 mm. So the actual width is scaled as:

$$\text{Real Width} = \max_{I \in [1, m]} (y_{RI} - y_{LI}) / 230 \text{ mm.}$$

### 2.3 Validation of Extracted Weld Pool Boundary

Figure 2.19 shows the actual welding seam and the corresponding weld pool boundary extraction results under varied welding speeds. The images are collected as the welding process reaches the steady state when the weld pool geometry can exactly reflect the welding situation of the desired speed. In each case of Figure 2.19, six processed images are chosen randomly and displayed from all the recorded frames. It is clear that there only exist small variations of the extracted boundaries (bright contour in Figure 2.19), which matches the expected results of the constant-velocity welding.

To validate the accuracy of the edge detection, the calculated widths from 30 continuous frames of the different welding speed are retrieved to compare with the actual experimental weld pool widths, and plotted in Figure 2.20. In Figure 2.20, the width variations of the different cases owe to the different laser power distribution. The fast welding speed makes less laser energy stay on the same welding spot so that the formed size of the weld pool shrinks. On the other hand, the actual width value was measured from both the top view (Figure 2.21) and the cross-section view (Figure 2.22) of the weld pool by an optical microscope. Interestingly, the polished and eroded cross-section view provides a more exact measurement result. By synthesizing the measured results of the width, the average values of all the welding speeds are summarized in Table 2.3. The relative error between the monitored value and the measurement is less than 8%, which means that the monitoring system and the proposed algorithm are effective for on-line weld pool monitoring.



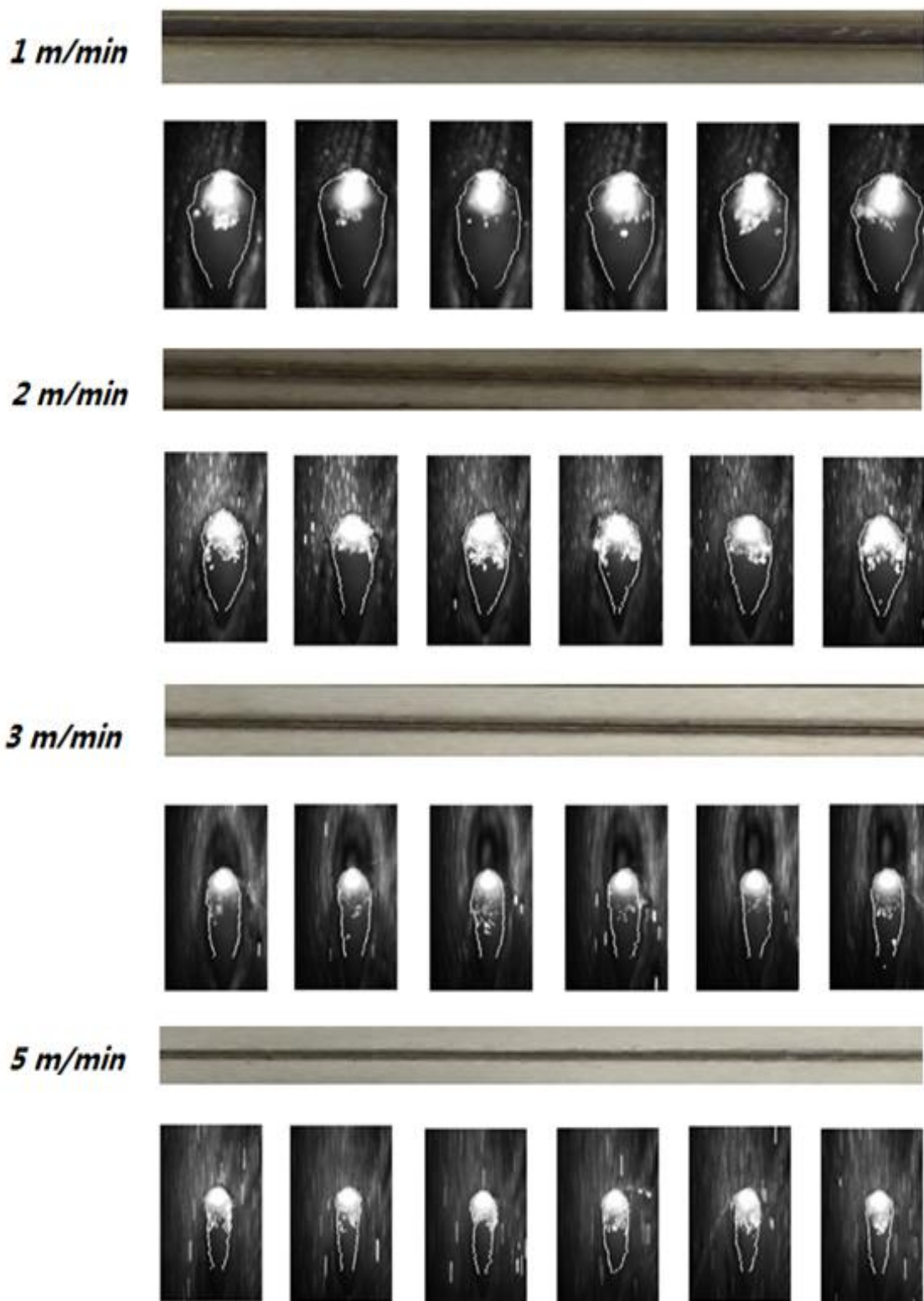


Figure 2.19. Real weld seam and corresponding extracted weld pool geometry.

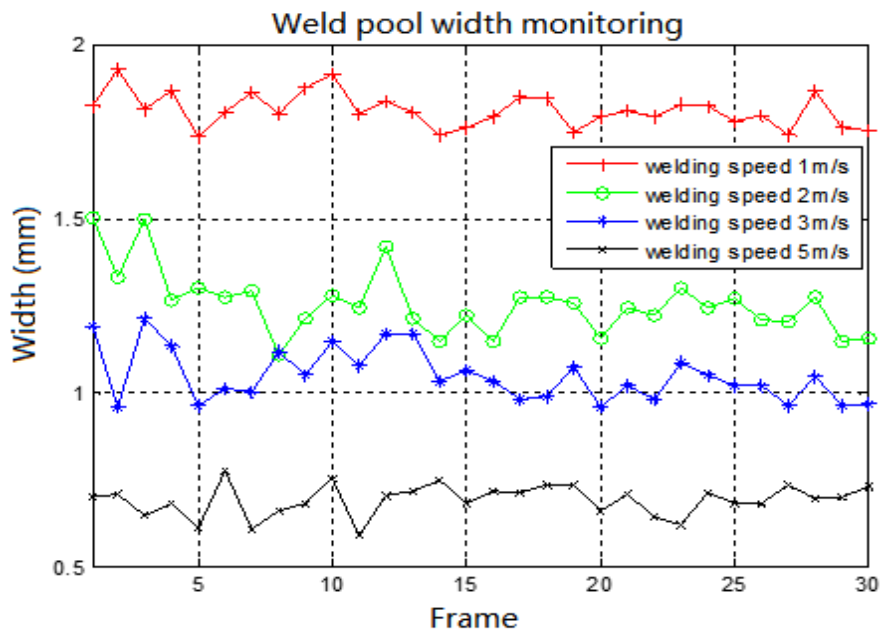


Figure 2.20. Calculated weld pool width.

Table 2.3. Average of weld pool width.

No.	Welding speed	Average of monitoring	Average of Measurement
1	1 m/min	1.8156 mm	1.784 mm
2	2 m/min	1.2519 mm	1.361mm
3	3 m/min	1.0494 mm	1.010mm
4	4 m/min	0.6767 mm	0.710mm

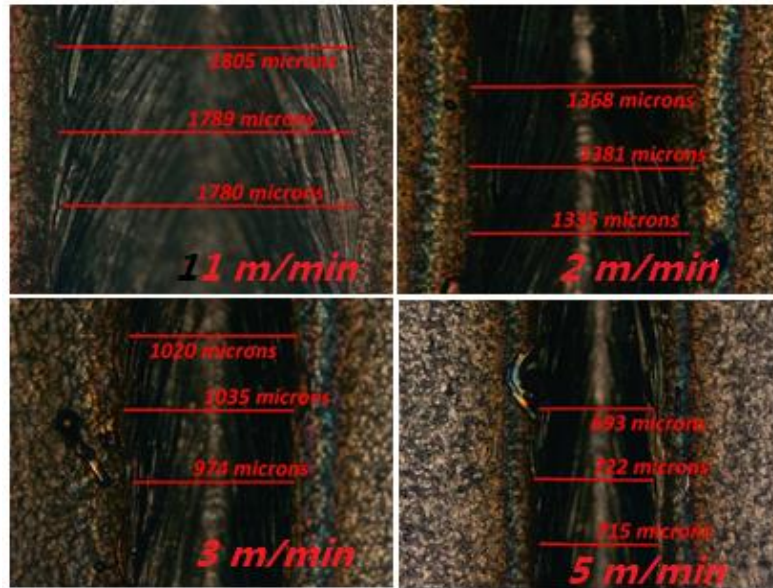


Figure 2.21. Top view of welding seam.

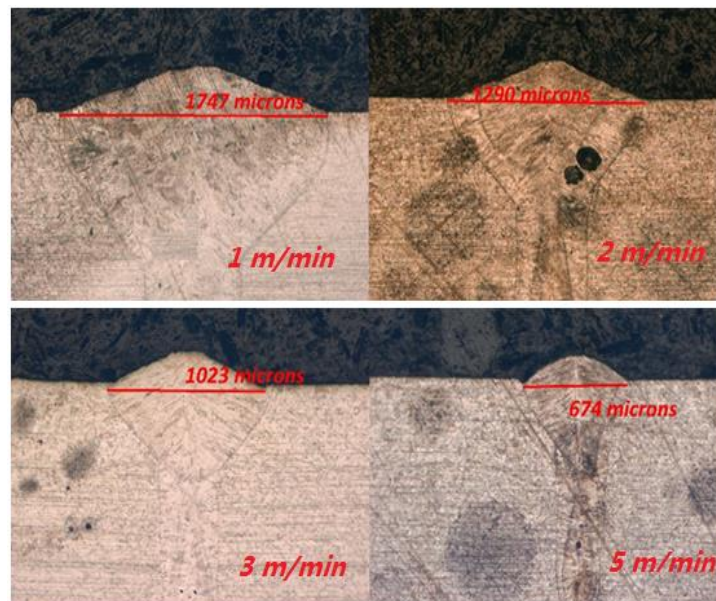


Figure 2.22. Cross-section view of weld pool.

Additionally, to further validate the extracted weld pool geometry and also to establish the correlations between the weld pool profile and the inherent dynamic

parameters of the keyhole welding, a well-developed three dimensional transient model for keyhole welding [11] is used to predict weld pool geometry. The model has taken into account the transport phenomena in the molten pool and keyhole plume, as well as the complicated boundary conditions on the sharp keyhole wall. The model is based on the sharp interface formulation and therefore the temperature on the keyhole wall and weld pool region can be accurately calculated.

In this model, the free interface between the condensed region (including liquid and solid phases) and the non-condensed region (including metallic vapor and ambient gas), a part of which is the keyhole wall, is tracked by the solution of the Level-set equation:

$$\frac{\partial \varphi}{\partial t} = - \left( \vec{V} + \frac{M_{evap}}{\rho_v} \cdot \vec{N} \right) \cdot \nabla \varphi. \quad (2.1)$$

Here  $\varphi$  is the LS value, which is defined to be zero at the interface of interest. Any points off the interface will have the LS value being the signed distance from this point to the interface, with the sign being positive in the non-condensed region and negative in the condensed region. The source term on the Right Hand Side (RHS) of the equation calculates the normal velocity of the interface, which includes two components. The first one is due to the local convection flow  $\vec{V}$ , and the second one is due to the surface recession induced by evaporation mass loss. Here  $M_{evap}$  is the mass evaporation rate and  $\rho_v$  is the vapor density. The transport phenomena in both the condensed and non-condensed regions are calculated based on the conservation equations of mass, momentum, energy and chemical species ((2.2) ~ (2.5)):

$$\frac{\partial}{\partial t}(\rho) + \nabla \cdot (\rho \vec{V}) = 0 \quad (2.2)$$

$$\frac{\partial}{\partial t}(\rho \vec{V}) + \nabla \cdot (\rho \vec{V} \vec{V}) = +\nabla \cdot (\mu \nabla \vec{V}) - \nabla p - \frac{\mu}{K} \vec{V} + \rho_r \vec{g} \beta_T (T - T_r) + \frac{\partial \gamma}{\partial T} \nabla_s T \delta_m(\varphi) \quad (2.3)$$

$$\frac{\partial}{\partial t}(\rho h) + \nabla \cdot (\rho \vec{V} h) = \nabla \cdot (k \nabla T) \quad (2.4)$$

$$\frac{\partial}{\partial t}(\rho Y) + \nabla \cdot (\rho \vec{V} Y) = \nabla \cdot (D \rho \nabla Y). \quad (2.5)$$

In the above equations,  $\rho$  is the density,  $\vec{V}$  is the velocity,  $\mu$  is the viscosity,  $K$  is the isotropic permeability expressed by the Kozeny-Carman equation,  $\rho_r$  is the reference density at the reference temperature  $T_r$ ,  $\beta_T$  is the thermal expansion coefficient,  $\nabla_s \gamma$  is the thermo-capillary force,  $\delta_m(\varphi)$  is the modified delta function,  $h$  is the material enthalpy,  $k$  is the thermal conductivity,  $f_s$  is the fraction of solid phase in a control volume,  $Y_i$  is the mass fraction of the  $i$ -th species, and  $D_i$  is the mass diffusion coefficient for the species. The boundary conditions on the interface consisting of sharp jump of temperature, heat flux, fluid velocity and pressure are discussed completely in the work [11].

Figure 2.23 shows the combined view of the monitored weld pool and the modeling result with the welding speed of 2 m/min. For the model, since the melting point of the material is 1670K, the boundary of the weld pool is approximated as the isotherm of 1670K. The welding conditions are exactly the same as the actual experiments. As can be seen, the profiles of the weld pool and the keyhole are quite close. The extracted weld pool boundary has been validated by the multi-physics modeling of keyhole welding.

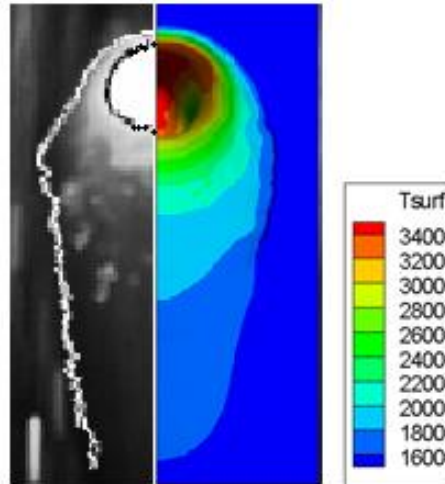


Figure 2.23. Combined view of monitored weld pool and modeling result for stainless steel.

The effectiveness of proposed image processing method has been verified as discussed. Especially, the algorithm is proved to be tolerant to the undesired imaging noises introduced by the illumination during the welding process with the base material of 304 stainless steel. To test the expansibility of the proposed algorithm in a general application, some implementations of the algorithm are explored. The algorithms developed for the tail part and head part can also be used to detect the weld pool boundary when base material used is magnesium alloys AZ31B. Although many image features of welding with magnesium alloys are different, the weld pool boundaries (bright profiles) of them could still be extracted successfully, as shown in Figure 2.24 and Figure 2.25. The chemical composition of magnesium alloys AZ31B is shown in Table 2.4. Further, the combined view of the numerical simulation result and extracted weld pool boundary of magnesium alloys is shown as Figure 2.26.

Table 2.4. Chemical composition of magnesium alloy AZ31B.

Element	Al	Zn	Mn	Si	Cu	Ca	Fe	Ni	Mg
Portion(%)	2.5-3.5	0.7-1.3	0.2	0.05	0.05	0.04	0.005	0.005	balance

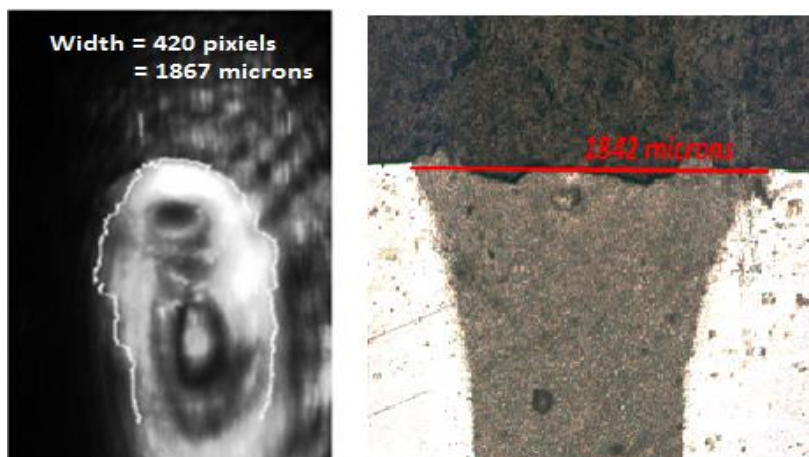


Figure 2.24. Boundary extraction for magnesium alloys AZ31B (800W, 2 m/min).

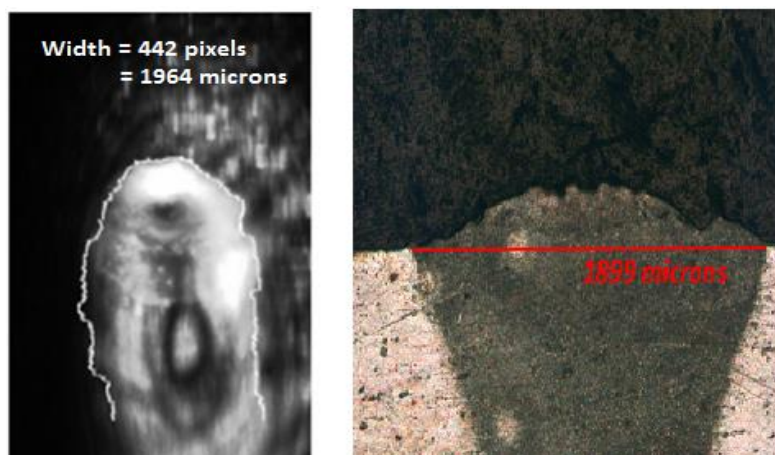


Figure 2.25. Boundary extraction for magnesium alloys AZ31B (900W, 2 m/min).



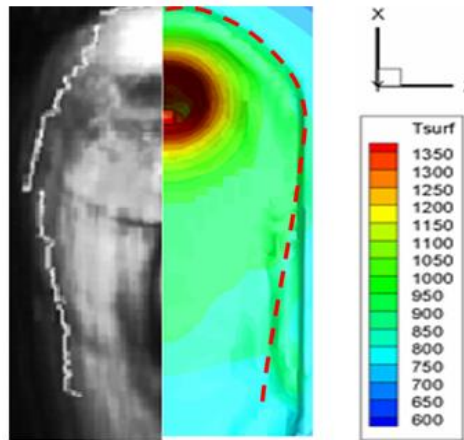


Figure 2.26. Combined view of monitored weld pool and simulation result for magnesium alloys (900W, 2 m/min).

In addition, Figure 2.27 shows the extracted boundaries of the weld pools on the different welding materials with using the algorithms of this work. The images were captured by the other similar setups [16, 17]. In Figure 2.27 (a), the bright dots are the extracted keyhole edge and weld pool edge of the welding on a 2mm thin 304 stainless steel without any illuminations. Figure 2.27 (b) shows the extracted contour of the weld pool by the white curve and the edge of keyhole by the black circle in the Zn-coated steel sheet keyhole welding. The image processing results in Figure 2.27 are pretty close to the recognition of weld pool by the human vision. So the developed algorithms in this work prove to be effective for the in-process weld pool monitoring system.



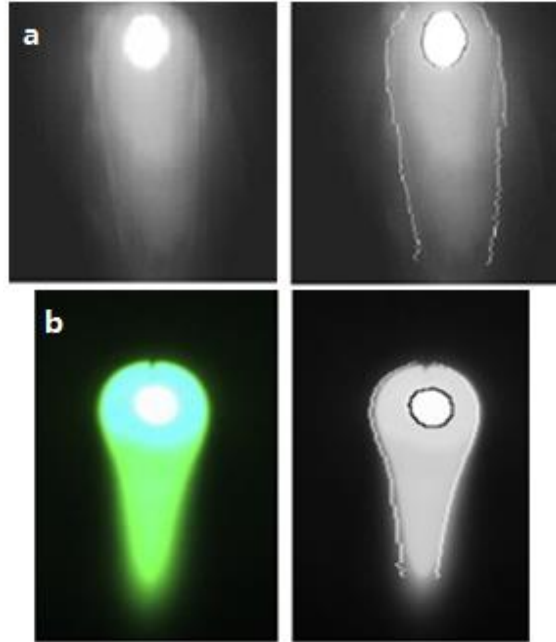


Figure 2.27. Extracted boundary of other cases.

## CHAPTER 3. ESTIMATION OF KEYHOLE GEOMETRY AND PREDICTION OF WELDING DEFECTS

In this chapter, the coaxial monitoring system is used to detect the keyhole shape from the top side. To approximate the keyhole dynamics in more straightforward and efficient manner under different welding conditions, a data-based static radial basis function neural network (RBFNN) is trained in order to establish the relationship among different welding parameters, system measurements and unobservable keyhole dynamics. Further, a dynamic RBFNN identification method [41] is used to estimate the penetration depth and keyhole front tilting angle for the transient state welding when some welding conditions change suddenly. The purpose of using this observer is to estimate the change of weld pool geometry due to unknown reasons, such as the nonuniformity of work material and absorptivity changes, so that a feedback welding control system can be design. Lastly, based on the visual monitoring system, two approaches are proposed to estimate in-process welding porosities.

### 3.1 Methodology of Estimating Keyhole Dynamics

#### 3.1.1 Radial Basis Function Neural Network

Keyhole dynamics is very important in the keyhole welding process since it can directly impact welding quality. However, an accurate mathematical model of the keyhole dynamics is not readily available. Thus, in this section, the application of a radial

basis function neural network is introduced to identify the keyhole dynamics. In system identification, the output of RBFNN is a linear combination of radial basis functions of the inputs and neuron parameters.

Given a continuous function  $F: R^+ \rightarrow R$ , and points  $\{\mathbf{X}_j^c: j = 1, \dots, p\}, \mathbf{X}_j^c \in R^+$ , the function  $F$  can be defined using radial basis functions as [41]:

$$t_p(\mathbf{X}) = \sum_{j=1}^p \lambda_j^p \Phi(|\mathbf{X} - \mathbf{X}_j^c|) + \lambda_0^T \mathbf{X} \quad (3.1)$$

where,  $|\cdot|$  is the Euclidean norm.  $\Phi(\cdot)$  is the radial basis function whose value depends only on the distance from the origin.  $\mathbf{X}$  is the input vector. The vector  $\mathbf{X}_j^c$  contains the centers of the basis function, which are determined by the training algorithm. The parameters  $\lambda_j^p$  are the weights between the nodes of basis function and output layer, and  $\lambda_0^T$  is the weight for the linear term. The value  $p$  is the number of basis functions in the neural network. The goal of using RBFNN is to reduce the errors between  $F(\mathbf{X})$  and  $t_p(\mathbf{X})$  by choosing the proper coefficients of  $\lambda_j^p$  and  $\lambda_0^T$ . The structure of RBFNN is shown in Figure 3.1.

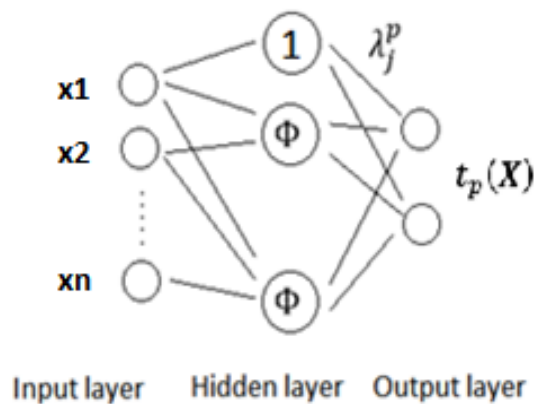


Figure 3.1. Schematic diagram of RBFNN.

### 3.1.2 Static RBFNN for Keyhole Dynamic

In order to generate a dynamic RBFNN to approximate keyhole dynamics in the transient state of keyhole welding, a static RBFNN is first developed to capture the correlation between welding parameters and keyhole geometric features. Because the welding speed range is from 1 m/min to 4 m/min in this work, the detected keyhole boundary is quite similar to a circle. Thus the keyhole diameter is used as a measurable keyhole feature. The inputs of the proposed static RBFNN include laser power, welding speed, and focal diameter, as well as keyhole diameter. The outputs consist of the penetration depth and keyhole front tilting angle. The schematic of the static RBFNN is shown in Figure 3.2. The radial basis function used is the Gaussian function, as shown in equations (3.2) and (3.3).  $\mathbf{X}$  and  $\mathbf{X}_j^c$  have been defined in section 3.1.1.

$$\Phi(r) = \exp(-r^2) \quad (3.2)$$

$$r = |\mathbf{X} - \mathbf{X}_j^c|. \quad (3.3)$$

The noteworthy point of the static RBFNN in Figure 3.2 is the scaling factor between the input data and hidden neurons. To guarantee the accuracy of the neural network, the scaling factors are utilized to map all the inputs to the same range, from 0 to 1. Considering the upper limit of the laser power as 1000 W and the maximum welding speed used as 4 m/min, the scaling factors for laser power, welding speed, focal diameter and keyhole diameter are respectively 0.001, 0.1, 0.001 and 1. The orthogonal least square genetic algorithm (OLSGA) [43] is adopted to train this static RBFNN.

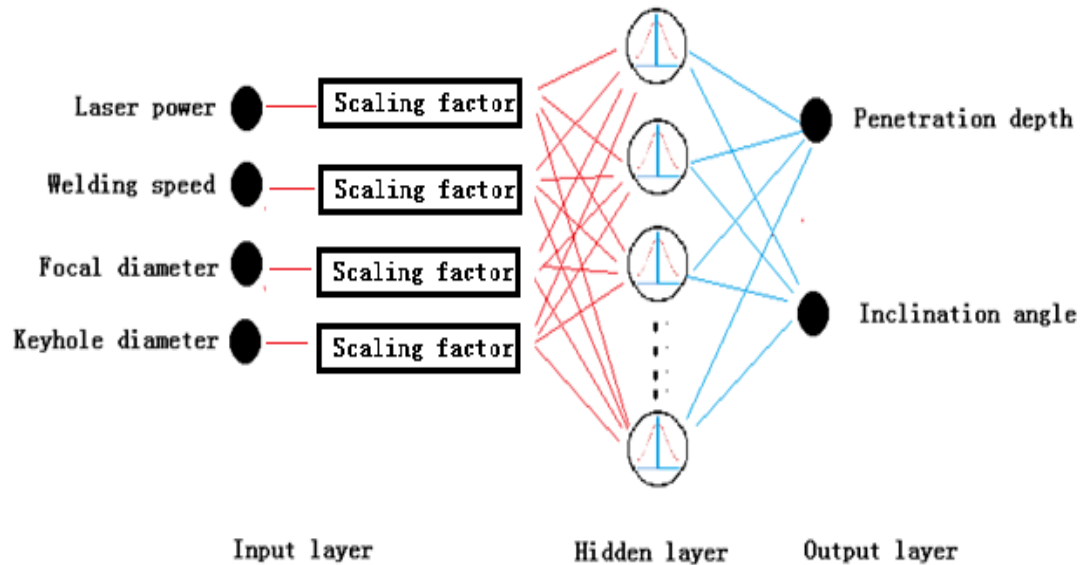


Figure 3.2. Static radial basis function neural network for keyhole dynamics.

### 3.1.3 Dynamic RBFNN for Keyhole Dynamic Estimation

In the welding process, although the well-trained static RBFNN is able to approximate the penetration depth and keyhole inclination angle in steady state welding, the keyhole dynamics in transient state welding cannot be predicted. Therefore, a dynamic RBFNN model is proposed to approximate the keyhole dynamic process with three state variables: keyhole diameter, penetration depth and keyhole inclination angle. Among these three, the keyhole diameter is a measurable state variable, but the other two are unmeasurable. The dynamic model is illustrated in Figure 3.3. In this dynamic model, the input includes both the welding parameters and the past values of three state variables.

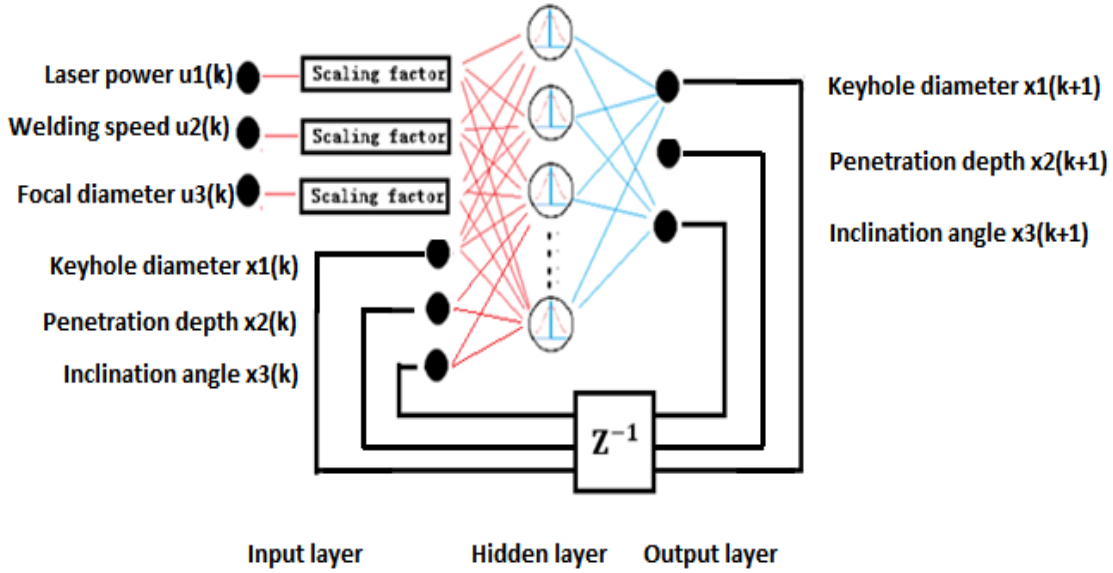


Figure 3.3. Dynamic radial basis function neural network model for keyhole dynamics.

In modeling the dynamic system, the neural network approach [41] is to generate an approximation through the input-output measurements. Once data is collected over a range of initial conditions for several experiments, the neural network must be trained to properly approximate the system dynamics. An unknown plant is described by:

$$\mathbf{x}_{k+1} = f(\mathbf{x}_k, \mathbf{u}_k) + \mathbf{w}_k \quad (3.4)$$

$$\mathbf{y}_k = h(\mathbf{x}_k) + \mathbf{v}_k \quad (3.5)$$

where state vector  $\mathbf{x}_k$  is n-dimensional and the output vector  $\mathbf{y}_k$  is assumed as m-dimensional. State and measurement noise vectors  $\mathbf{w}_k$  and  $\mathbf{v}_k$  are assumed to be independent Gaussian white processes with zero mean. The RBFNN then approximates the plant dynamics for each experiment  $i$  as:

$$\mathbf{x}_{k+1}^i = [\Lambda \quad \Lambda_0] \begin{bmatrix} \Psi(\mathbf{X}_k^i) \\ \mathbf{X}_k^i \end{bmatrix} + \mathbf{w}_k^i \quad (3.6)$$

$$\mathbf{z}_k^i = \mathbf{x}_k^i + \zeta_k^i \quad (3.7)$$

where  $\mathbf{X}_k^i$  contains the state variables and the input for experiment  $i$ , and  $\Psi(\mathbf{X}_k^i) = [\Phi_1(\mathbf{X}_k^i), \dots, \Phi_p(\mathbf{X}_k^i)]^T$  contains the basis functions corresponding to  $p$  centers.

Each row of the matrices  $\Lambda$  and  $\Lambda_0$  correspond to an element of the approximated vector function  $\hat{f}(\cdot)$ . If define the vector  $\theta_j^T$  as the  $j$ th row of the matrix  $[\Lambda \ \Lambda_0]$ , then (3.6) can be rewritten as:

$$\mathbf{x}_{k+1}^i = \begin{bmatrix} \Psi_{ik}^T & 0 & \cdots & 0 \\ 0 & \Psi_{ik}^T & \cdots & 0 \\ \vdots & \vdots & \ddots & \vdots \\ 0 & \cdots & 0 & \Psi_{ik}^T \end{bmatrix} \begin{bmatrix} \theta_1 \\ \theta_2 \\ \vdots \\ \theta_n \end{bmatrix} + \mathbf{w}_k^i. \quad (3.8)$$

For  $i = 1, \dots, M$  experiments, where the notation  $\Psi_{ik}^T \triangleq [\Psi^T(\mathbf{X}_k^i) \ \mathbf{X}_k^{iT}]$ . Finally, to simplify (8), further define  $\Theta = [\theta_1 \ \cdots \ \theta_n]^T$  and combine all  $M$  experiments, a system with  $Mn$  hyperstate variables and  $np$  parameters is described as:

$$\boldsymbol{\eta}_{k+1} = \xi_k(\boldsymbol{\eta}_k, \mathbf{u}_k)\Theta + \mathbf{w}_k \quad (3.9)$$

$$\boldsymbol{\gamma}_k = \boldsymbol{\eta}_k + \boldsymbol{\zeta}_k. \quad (3.10)$$

Here  $\boldsymbol{\eta}_k = [x_{1k}^1 \ x_{1k}^2 \ \cdots \ x_{1k}^M \ x_{2k}^1 \ \cdots \ x_{nk}^M]^T$ ,  $\boldsymbol{\gamma}$  and  $\boldsymbol{\zeta}$  denote output and measurement noise respectively. The matrix  $\xi_k(\boldsymbol{\eta}_k, \mathbf{u}_k)$  is of dimension  $Mn \times np$  and is defined as:

$$\xi_k(\boldsymbol{\eta}_k, \mathbf{u}_k) = \begin{bmatrix} \begin{pmatrix} \Psi_{1k}^T \\ \vdots \\ \Psi_{Mk}^T \end{pmatrix} & 0 & \cdots & 0 \\ \vdots & \vdots & \cdots & \vdots \\ 0 & \cdots & 0 & \begin{pmatrix} \Psi_{1k}^T \\ \vdots \\ \Psi_{Mk}^T \end{pmatrix} \end{bmatrix}. \quad (3.11)$$

The goal of the training algorithm is restated as determining the values of the matrix  $\hat{\Theta}$  such that the error between the measurements  $\mathbf{y}_k$  and the output of the system estimate  $\hat{\xi}_k(\boldsymbol{\eta}_k, \mathbf{u}_k)$  is minimized. The recursive update equation of  $\hat{\Theta}$  becomes:

$$\hat{\Theta}_{N+1} = \hat{\Theta}_N + R_N \hat{\xi}_{N-1}^T [I + \hat{\xi}_N R_N \hat{\xi}_{N-1}^T]^{-1} \times [\mathbf{y}_{N+1} - \hat{\xi}_N \hat{\Theta}_N] \quad (3.12)$$

$$R_{N+1} = R_N - R_N \hat{\xi}_{N-1}^T [I + \hat{\xi}_N R_N \hat{\xi}_{N-1}^T]^{-1} \hat{\xi}_N R_N. \quad (3.13)$$

The faster convergence of the training algorithm (3.12) and (3.13) can be obtained by choosing  $R_0 = \sigma I$  with a sufficiently large value of  $\sigma$ . Approximation of the system output equations can be carried out similarly.

A state estimator gain was then designed for the RBFNN to adapt its state estimations based on predicted states and actual measured states. For convenience, we write the approximated system using the RBFNN as:

$$\mathbf{x}_{k+1} = f'(\mathbf{x}_k, \mathbf{u}_k) + F\mathbf{x}_k + b\mathbf{u}_k + \mathbf{w}_k \quad (3.14)$$

$$\mathbf{y}_k = h'(\mathbf{x}_k) + H\mathbf{x}_k + \mathbf{v}_k. \quad (3.15)$$

The estimated states can then be determined by the following state estimator equation,

$$\hat{\mathbf{x}}_{k+1} = f'(\hat{\mathbf{x}}_k, \mathbf{u}_k) + F\hat{\mathbf{x}}_k + b\mathbf{u}_k + K_k[\mathbf{y}_k - h'(\hat{\mathbf{x}}_k) - H\hat{\mathbf{x}}_k]. \quad (3.16)$$

The minimum variance gain  $K_k^*$  can then be calculated as:

$$K_k^* = F\hat{P}_k H^T \left[ \left( \frac{l_4}{l_1} + \frac{l_5}{l_1} \text{Tr}(\hat{P}_k) \right) I + \frac{1}{l_1} V + H\hat{P}_k H^T \right]^{-1}. \quad (3.17)$$

And the estimated covariance of the states  $\hat{P}_k$  follows the update equation:

$$\begin{aligned} \hat{P}_{k+1} = & l_1(F - K_k H)\hat{P}_k(F - K_k H)^T + \left( l_2 + l_3 \text{Tr}(\hat{P}_k) \right) I + \left( l_4 + l_5 \text{Tr}(\hat{P}_k) \right) K_k K_k^T + \\ & W + K_k V K_k^T. \end{aligned} \quad (3.18)$$



In (3.17) and (3.18),  $V$  is the covariance matrix of the measurement noise,  $W$  is the covariance matrix of the system noise.  $Tr(\hat{P}_k) = \sum_{i=1}^n \hat{P}_{i,i}$ , which is the sum of the diagonal entries of the estimated state covariance matrix  $\hat{P}_k$ , and the values  $l_{1-5}$  are defined as:

$$l_1 = 1 + a + d + 2e_f + e_h \quad (3.19)$$

$$l_2 = ne_f(2 + a + d + e_f + e_h)$$

$$l_3 = a(a + d + e_f + e_h)$$

$$l_4 = me_f(1 + a + d + e_f + e_h)$$

$$l_5 = a + d + ad + d^2 + e_f d + e_h d.$$

The constants  $e_f$  and  $e_h$  are the maximum error in approximating the states and measurements respectively, and are determined by the training algorithm. The constants  $a$  and  $d$  are the Lipschitz constants, and are defined as:

$$\|f'(\mathbf{x}_k, \mathbf{u}_k) - f'(\mathbf{x}_k + \boldsymbol{\delta}_k, \mathbf{u}_k)\|_\infty \leq a \|\boldsymbol{\delta}_k\|_\infty \quad (3.20)$$

$$\|h'(\mathbf{x}_k + \boldsymbol{\delta}_k) - h'(\mathbf{x}_k)\|_\infty \leq d \|\boldsymbol{\delta}_k\|_\infty. \quad (3.21)$$

Since the parameters appear in the RBFNN as a linear form, least squares estimation is possible. The state estimator is designed for use with the RBFNN and the gain matrix is derived on the basis of an upper bound covariance matrix. In addition, the consideration of approximation error in the estimation algorithm successfully minimizes filter divergence.

For the keyhole dynamics, the structure of the dynamic estimator is shown in Figure 3.4. The experiment number  $i$  is determined by the actual transient welding situations that are considered in the next section.

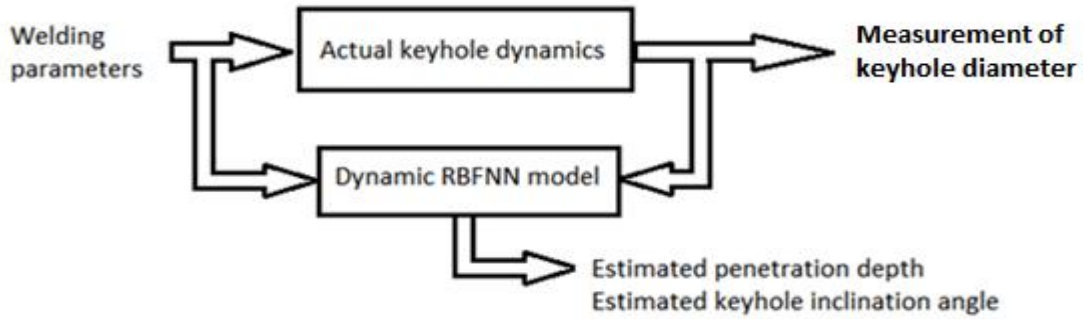


Figure 3.4. Structure of estimator based on RBFNN.

### 3.2 Data Collection and Static Neural Network Training

Since the training of static RBFNN is based on the input and output data, experiments are necessary to collect the data for training the neural network. In consideration of the range of interest for welding parameters, the experiments are designed as shown in Table 3.1. The focal diameter of the laser equipment is kept at 200  $\mu\text{m}$ , so it is not listed in Table 3.1, but should still be regarded as an input for the expandability of the proposed RBFNN.

Table 3.1. Designed experiments.

Experiment No.	Laser power	Welding speed	Experiment No.	Laser power	Welding speed
1	400 W	1 m/min	9	800 W	1 m/min
2	400 W	2 m/min	10	800 W	2 m/min
3	400 W	3 m/min	11	800 W	3 m/min
4	400 W	4 m/min	12	800 W	4 m/min
5	600 W	1 m/min	13	1000 W	1 m/min
6	600 W	2 m/min	14	1000 W	2 m/min
7	600 W	3 m/min	15	1000 W	3 m/min
8	600 W	4 m/min	16	1000 W	4 m/min

### 3.2.1 Detected Keyhole Diameters

The keyhole diameters are detected by the coaxial monitoring system, as shown in Figure 3.5. The average values of keyhole diameters under different welding parameters are plotted in Figure 3.6 and the corresponding captured images are summarized in Table 3.2. As can be seen, the change of keyhole size is not quite linear with respect to the change of welding condition. Generally, an increase in laser power or a decrease in welding speed makes the keyhole size larger.



Figure 3.5 Detected keyhole area and keyhole diameter.

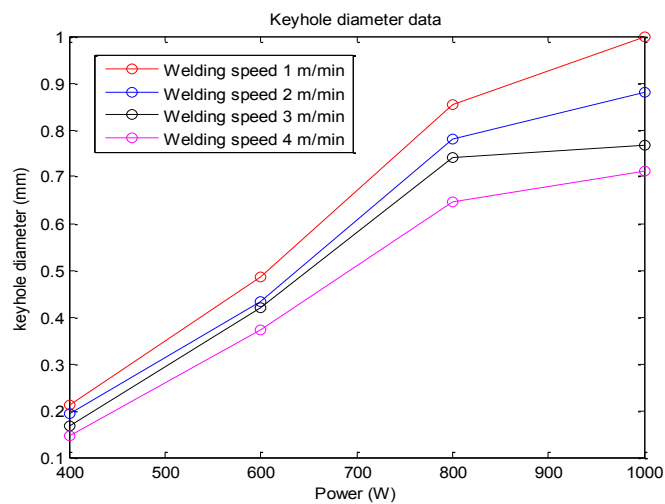
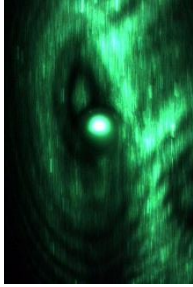
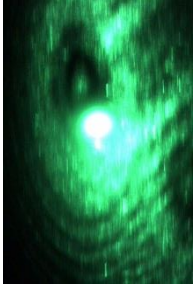
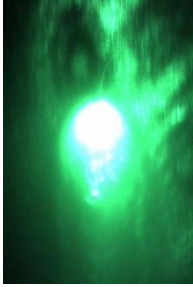
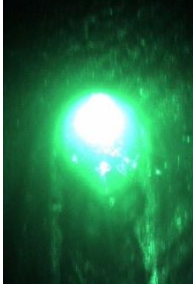
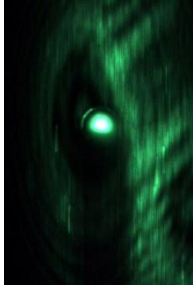
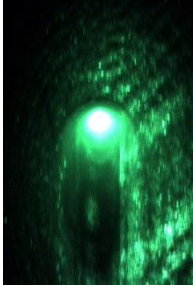
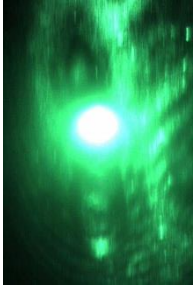
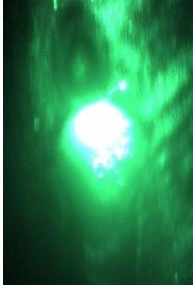
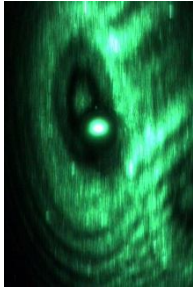
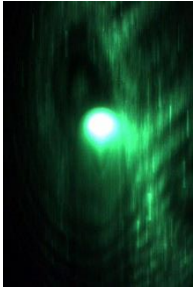

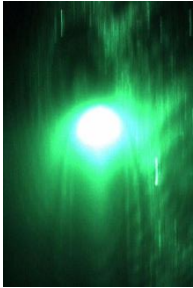
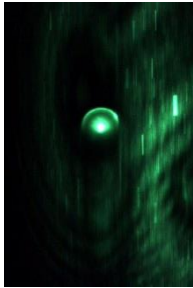
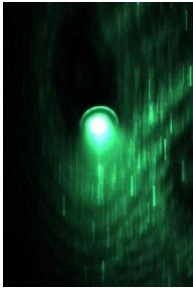
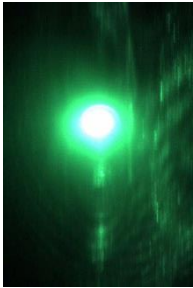
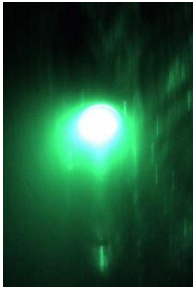


Figure 3.6. Keyhole diameters under different welding parameters.

Table 3.2. Average keyhole diameters from images: (150 pixels = 1 mm).

	400 W	600 W	800 W	1000 W
1 m/min	32 (0.213mm) 	73 (0.486mm) 	128(0.853mm) 	150 (1mm) 
2 m/min	29 (0.193mm) 	65 (0.433mm) 	117 (0.78mm) 	132 (0.88mm) 
3 m/min	25 (0.167mm) 	63 (0.42mm) 	111 (0.74mm) 	115 (0.767mm) 
4 m/min	22 (0.147mm) 	56 (0.373mm) 	97 (0.647mm) 	107 (0.713mm) 

### 3.2.2 Penetration Depth and Inclination Angle

The techniques for measuring penetration depth and inclination angle are different since both of them cannot be directly measured from the coaxial monitoring system. Therefore, the cross section view of the post-processed weld is used to realize the data collection. The cross section view perpendicular to the weld (Figure 3.7) provides sufficient information on the penetration depth. As for the inclination angle, the longitudinal cross section view (Figure 3.8) shows the angle clearly at the end of each weld. All the experimental data for the penetration depth and inclination angle are plotted in Figure 3.9.

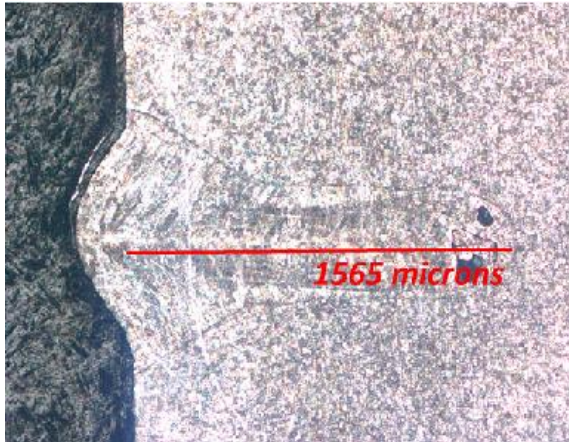


Figure 3.7. Cross section view to for penetration depth measurement (800 W, 2m/min).

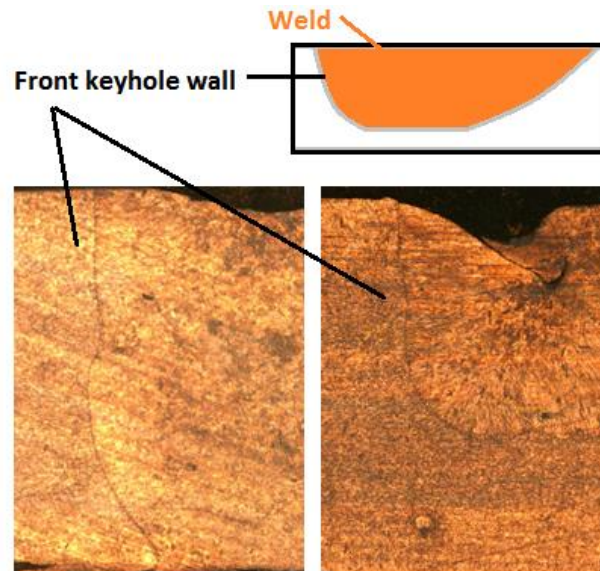


Figure 3.8. Cross-section view for keyhole inclination angle (Left: 1000 W, 1 m/min. Right: 1000 W, 2 m/min).

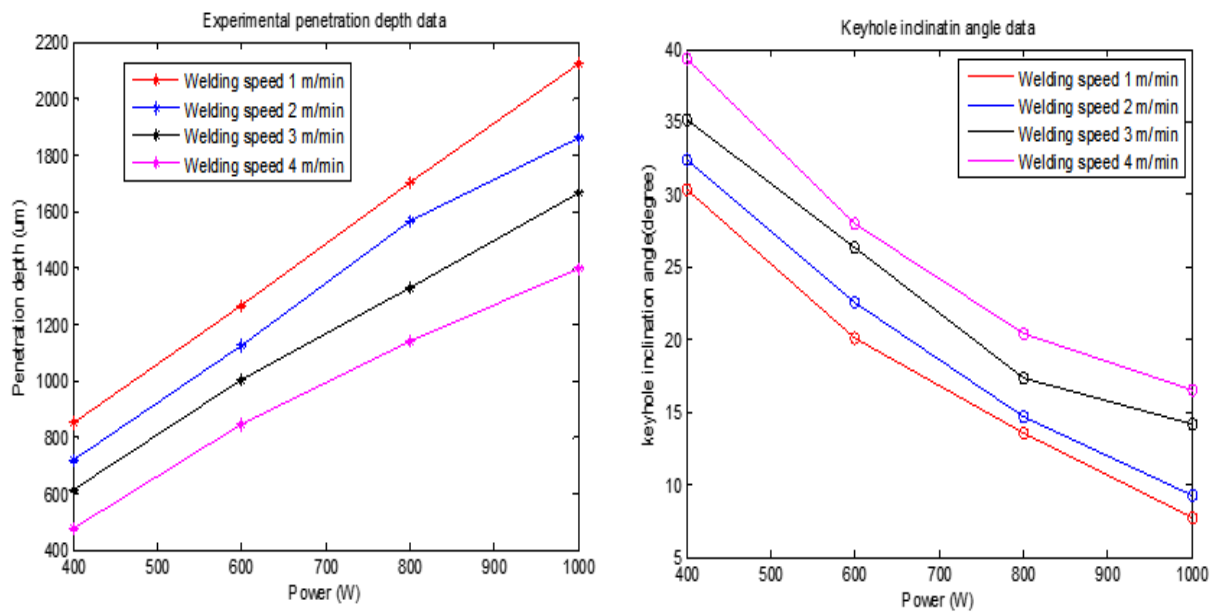


Figure 3.9. Experimental data for penetration depth (left) and inclination angle (right).

### 3.2.3 Training Results of Static RBFNN

To conduct off-line training, OLSGA [43] is utilized since it can better approximate the system features even when the data set is insufficient. This algorithm adds a significant radial basis function node at each iteration during training based on an error reduction measure using the orthogonal least square method, while the genetic algorithm provides a way of achieving a global optimum than other gradient-based search methods for the calculation of width and center of RBF in each iteration within the predefined upper and lower bounds of the search range. The training result for penetration depth is shown in Figure 3.10, while the training result for inclination angle is shown in Figure 3.11. From the error plots, it can be seen that both errors are very small, less than 1%, when compared to the actual data sets.

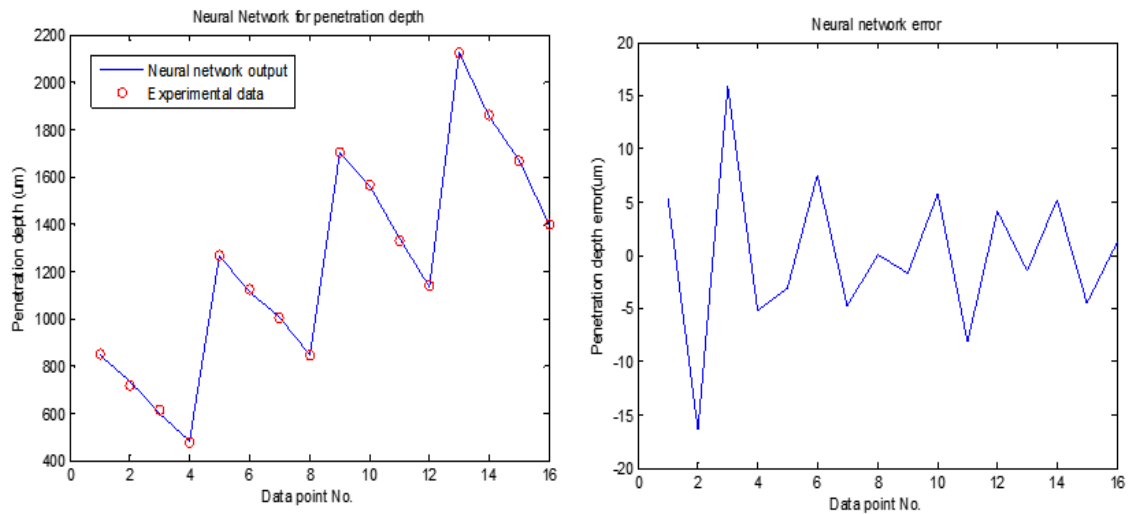


Figure 3.10. Training results and errors of penetration depth.

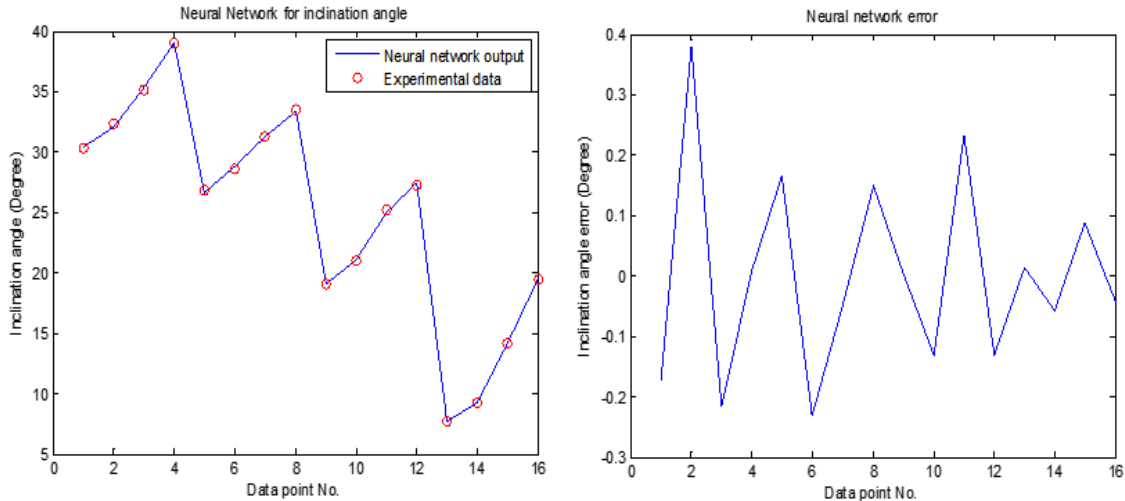


Figure 3.11. Training results and errors of inclination angle.

### 3.2.4 Testing of Static Neural Network

The well-trained static neural network covers the range of welding power from 400 W to 1000 W and the welding speed from 1 m/min to 4 m/min. To test the effectiveness of the static RBFNN, data other than the training sets are used. In this work, the test experiments are conducted with the laser power of 500 W and the welding speeds of 2 m/min, 3 m/min and 4 m/min. The comparisons between the actual results and neural network approximation are summarized in Table 3.3 and Table 3.4. The respective experimental results are also shown in Figure 3.12 (a) and Figure 3.12 (b). When compared with the test results, the errors of the neural network are all less than 3 %, which means this static neural network can be utilized to approximate correlations between the different welding parameters and keyhole geometries in the steady state welding process.



Table 3.3. Test data for penetration depth.

Power	Welding speed	Focal diameter	Keyhole diameter(mm)	Experimental keyhole depth ( $\mu\text{m}$ )	Neural Network keyhole depth ( $\mu\text{m}$ )
500 W	2 m/min	200 $\mu\text{m}$	0.35	981	1007.0
500 W	3 m/min	200 $\mu\text{m}$	0.324	889	866.2
500 W	4 m/min	200 $\mu\text{m}$	0.27	687	674.32

Table 3.4. Test data for inclination angle.

Power	Welding speed	Focal diameter	Keyhole diameter(mm)	Experimental Inclination angle ( $^{\circ}$ )	Neural Network Inclination angle ( $^{\circ}$ )
500 W	2 m/min	200 $\mu\text{m}$	0.35	30.6	31.86
500 W	4 m/min	200 $\mu\text{m}$	0.27	35.5	36.57

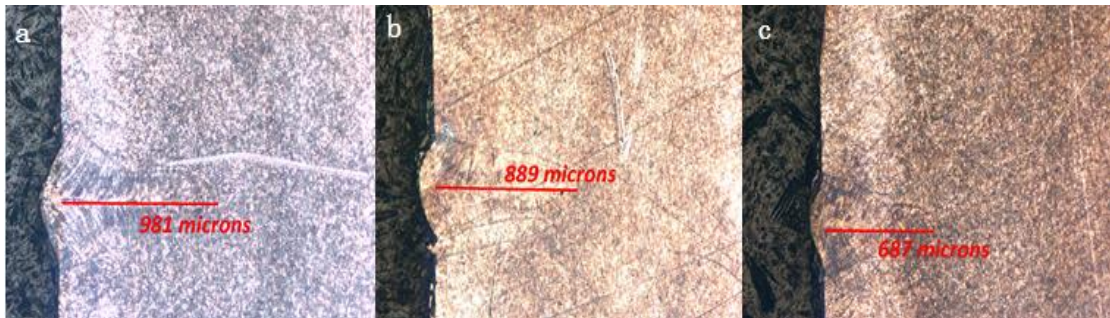


Figure 3.12 (a). Penetration depth of (a) 500 W, 2 m/min (b) 500 W, 3 m/min (c) 500 W, 4 m/min.

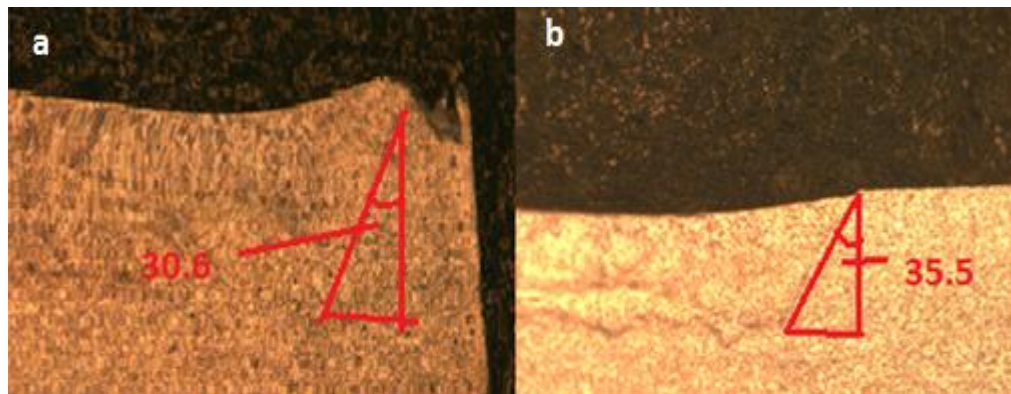


Figure 3.12 (b). Inclination angle of (a) 500 W, 2 m/min (b) 500 W, 4 m/min.

### 3.3 Dynamic RBFNN-based Observer for Keyhole Dynamic

#### 3.3.1 Data Training for Dynamic RBFNN

As for the dynamic laser welding process, the keyhole geometry is estimated based on the dynamic RBFNN shown in Figure 3.3. In this work, two groups of experiments are carried out for transient state laser welding. The first one suddenly changes laser power from 400 W to 1000 W (changing time is less than 1 ms) with a constant welding speed of 2 m/min. The second changes the welding speed from 2 m/min to 3 m/min with a constant acceleration rate of  $15 \text{ m/s}^2$  and laser power of 1000 W. The focal diameter used in the experiments is still  $200 \mu\text{m}$ . To train the dynamic neural network model, the transient data is obtained from the numerical model [8] with an output every 0.1 ms. Figure 3.13 shows the keyhole dynamic changes predicted by this numeric model with respect to time. The entire transient state process lasts 41 ms and 68 ms for the first and second case, respectively. The training results of the dynamic neural network are shown in Figure 3.14 (a) and Figure 3.14 (b). It is obvious that the trained RBFNN is capable of capturing the keyhole dynamics very well.

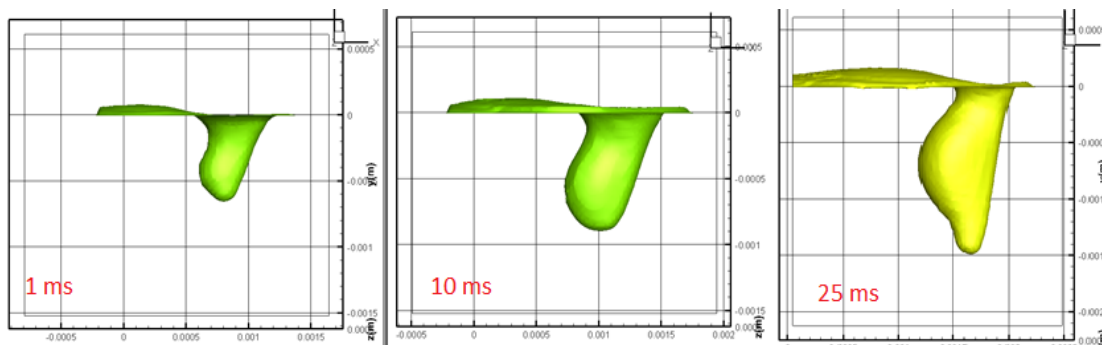


Figure 3.13. Training data from numerical simulations (Case of changing power).

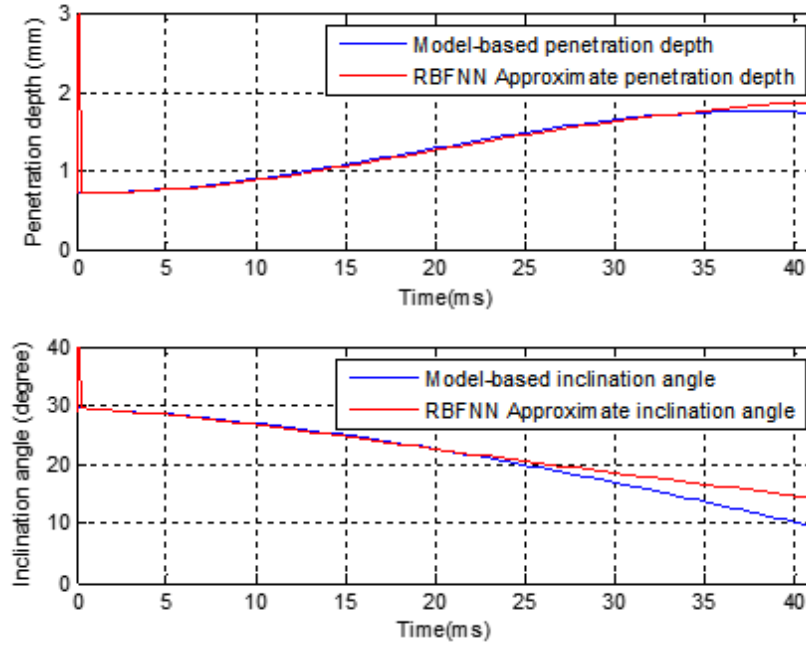


Figure 3.14 (a). Dynamic neural network training results for changing laser power.

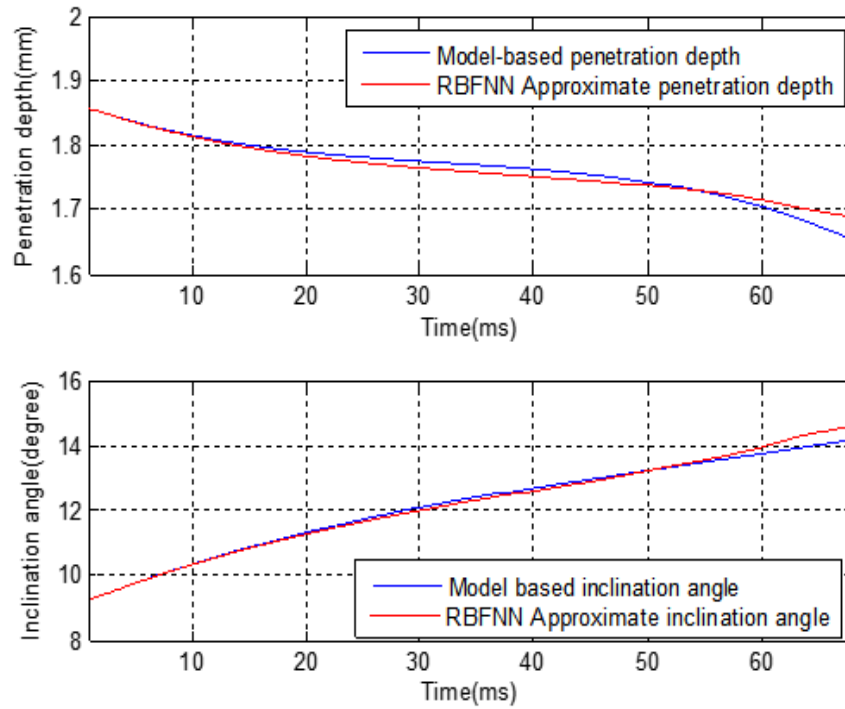


Figure 3.14 (b). Dynamic neural network training results for changing welding speed.

### 3.3.2 Estimation Results of Dynamic RBFNN Observer

After the training, the observer is used to estimate the penetration depth and inclination angle. The actual penetration depth from the cross section view along the centerline of the weld is compared with the estimated keyhole penetration depth. As shown in Figure 3.15, the red circles of the actual penetration depth are located very close to the blue line of estimated penetration depth. As for the keyhole inclination angle, the estimated results are compared to the actual model-based data in Figure 3.16, in which predicted inclination angle acceptably represents the actual experimental result. These results demonstrate the accuracy of keyhole dynamic estimation via the RBFNN-based observer.

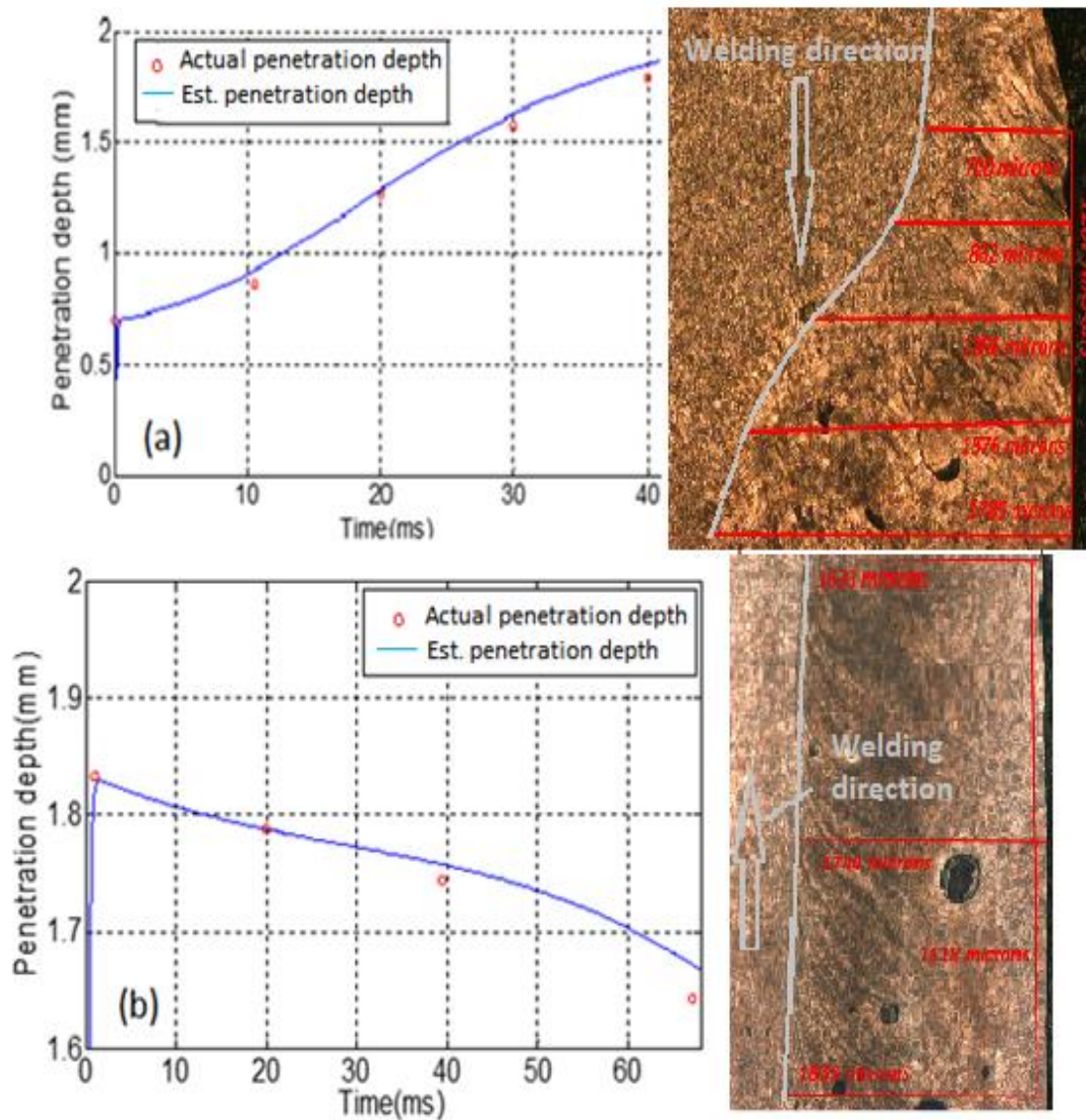


Figure 3.15. Comparison of estimated penetration depth and experimental results for (a) changing power (b) changing speed.

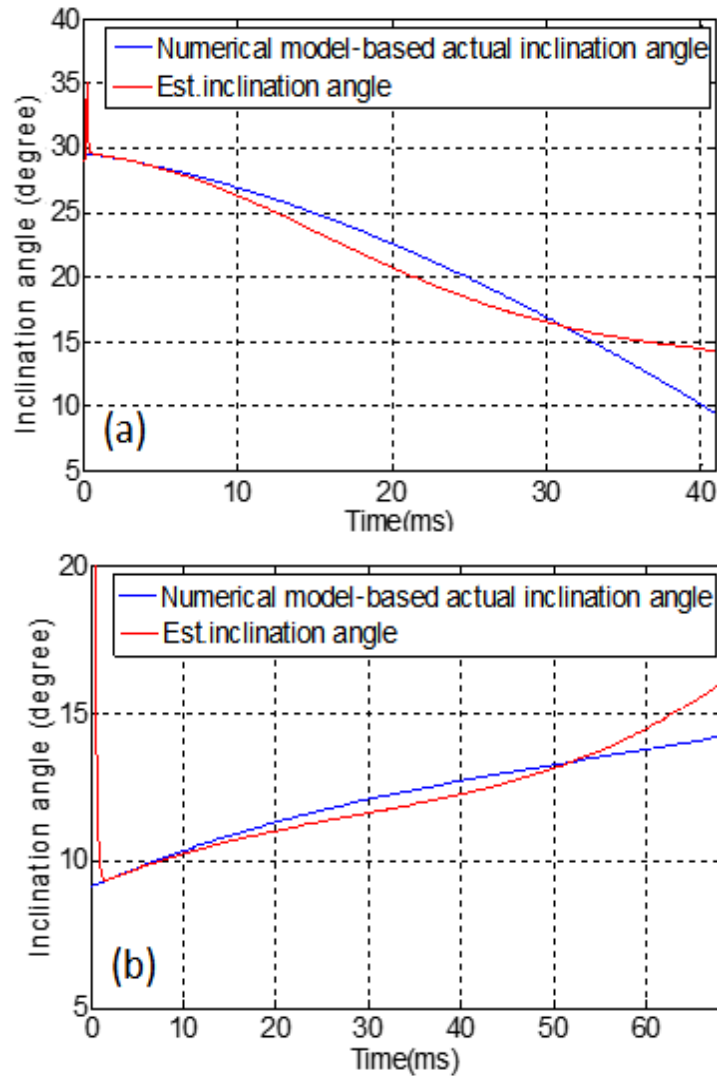


Figure 3.16. Comparison of numerical model-based actual angle and estimated angle (a) Changing power (b) Changing speed.

### 3.4 Prediction of Welding Defects

To predict the potential porosity and evaluate the welding quality, two approaches with the coaxial monitoring system are proposed, one of which is based on the predefined bound of variation and the other derived from the statistical analysis. As can be seen in the experimental results, the detected keyhole size has fluctuations even in the steady



state of welding. Under certain welding conditions, variations of the keyhole size exceed the preset range due to the possibility of a collapsed keyhole and porosities formed inside the weld pool. Through analyzing these imaging signals, welding porosities could be predicted in real time for both stainless steel 304 and magnesium alloy AZ31B.

**(1) Image binarization:** After capturing the images of the keyhole, the color images are converted to grey ones, which consist of all pixels with the greyness value from 0 to 255. For the welding of stainless steel, the brightest part of the captured image is the keyhole area. The threshold value for image binarization is chosen as 240. Thus, pixels with greyness value under 240 are reset to 0, while values above 240 are reset to 255, as shown in Figure 3.17. However, due to the difference of the absorptivity ratio of the green light, the keyhole for magnesium is darker than its surroundings, as marked out by red squares in Figure 3.18. The threshold value for image binarization of magnesium welding is chosen as 80 in the present work. The converted image and binarization results are also shown in Figure 3.18.

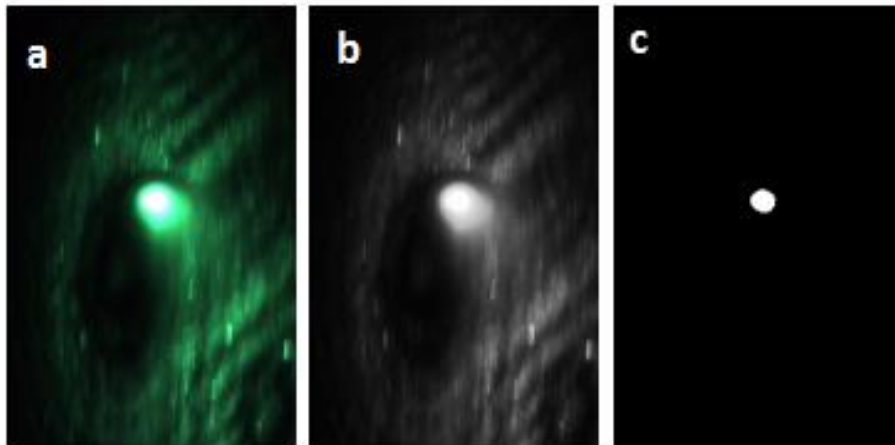


Figure 3.17. Keyhole area detection with stainless steel (a) Original image (b) Converted grey image (c) Binarized image.

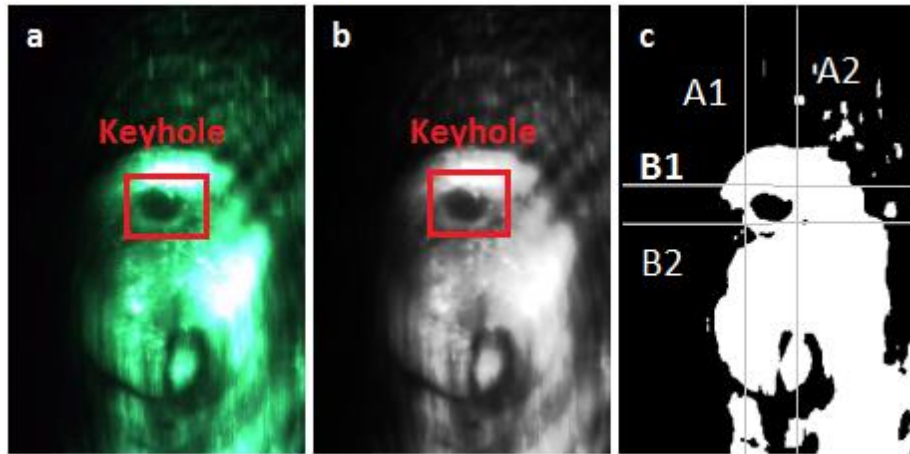


Figure 3.18. Keyhole area detection with magnesium alloy (a) Original image (b) Converted grey image (c) Binarized image.

**(2) Keyhole size determination:** To describe the keyhole size, the total pixel number of the keyhole area is used. For stainless steel, the binarization is able to clearly separate the keyhole from the background, and thus the pixel number  $N$  with greyness value of 255 is regarded as the size of the keyhole area. On the other hand, some additional locating techniques are necessary due to the noises of binarized magnesium images. The relative position of the keyhole center in an entire captured image is fixed since the monitoring system cannot be moved during the welding process; consequently, only the region bounded by lines A1, A2, B1 and B2 is considered, as shown in Figure 3.18 (c). From the actual experimental results, it is confirmed that no keyhole area is larger than this bounded region. The total pixel number with greyness value of 0 inside this pre-defined search area is used to determine the keyhole size as  $N$ .

**(3) Mean value, upper and lower bound:** After recording a series of keyhole images that contain  $K$  consecutive frames, the mean value of keyhole size is determined as

$$M = \frac{1}{K} \sum_{i=1}^K N_i.$$

In the experiment with stainless steel, the fluctuation below the 10%



is taken as a reasonable change of the keyhole size, and the upper and lower bounds are 1.1 M and 0.9 M respectively. When considering the more unstable properties of the magnesium alloy, fluctuation of keyhole size around the mean value less than 25% is assumed to be a reasonable change. Consequently, the upper and lower bounds for magnesium alloy are respectively 1.25 M and 0.75 M.

**(4) Experiment design for welding quality classification:** In the experiment design, different welding parameters are selected for resultant welds classified as either good welding or poor welding. The designed welding parameters are listed in Table 3.5 and Table 3.6. Through the cross sectional views of the post-processed welds, as illustrated in Figure 3.19 and Figure 3.20, the corresponding welding quality is also determined.

Table 3.5. Designed experiment parameters for stainless steel.

<b>Experiment No.</b>	<b>Laser power</b>	<b>Welding speed</b>	<b>Welding quality</b>
1	1000 W	1 m/min	Poor
2	1000 W	2 m/min	Poor
3	500 W	2 m/min	Good

Table 3.6. Designed experiment parameters for magnesium alloys.

<b>Experiment No.</b>	<b>Laser power</b>	<b>Welding speed</b>	<b>Welding quality</b>
1	700 W	0.9 m/min	Good
2	800 W	2 m/min	Poor
3	900 W	2 m/min	Poor

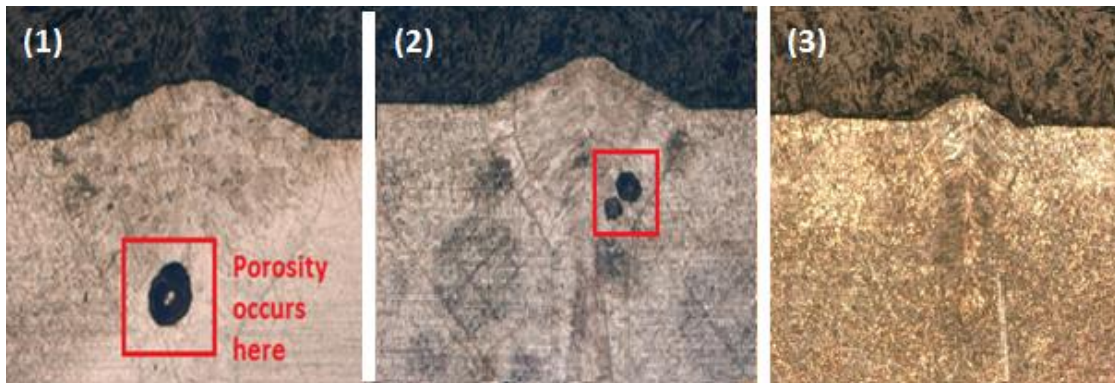


Figure 3.19. Horizontal cross section view of weld on stainless steel.

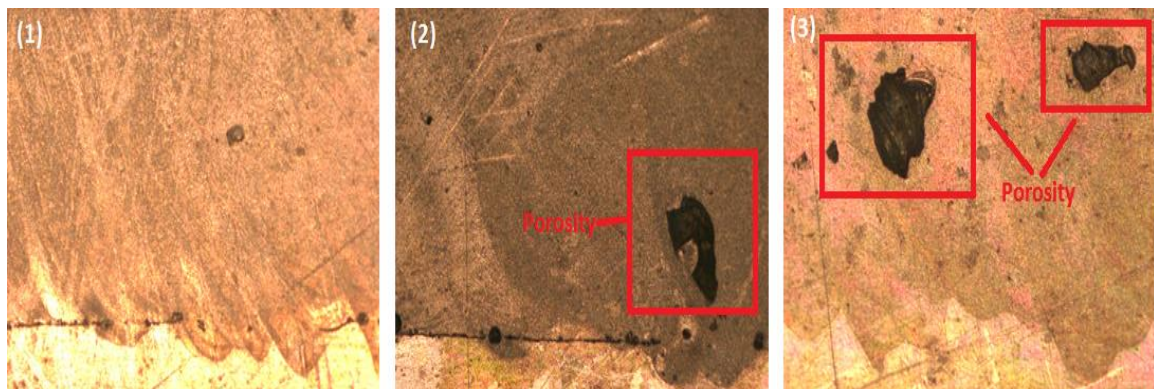


Figure 3.20. Longitudinal cross section view of weld on magnesium.

**(5) Porosity prediction method 1:** If there are calculated keyhole sizes located out of the lower and upper bounds, it means that the unusual keyhole changes happened in the welding process and there is a high chance of porosity formation in the base material. In Figure 3.21 (a) and (b) and Figure 3.22 (b) and (c), either many points are outside the pre-defined regions or sharp peaks occur in the plots, where the undesired points are all marked by red dots. On the other hand, all of the points are within the two bounds in Figure 3.21 (c) and Figure 3.22 (a), which means that few welding defects are

detected during the welding process. Therefore, the detected results from Figure 3.21 and Figure 3.22 accurately reflect the welding qualities summarized in Table 3.5 and Table 3.6.

**(6) Porosity prediction method 2:** As the variation of the keyhole size is a statistical process, the relative standard error (RSE) can be applied to get a more qualitative measure of the variance around the mean in estimating the welding quality, where  $RSE = \frac{\sigma(\text{Standard deviation})}{M(\text{Mean value})}$ . For the case in Figure 3.21,  $RSE_1 = 0.1006$  for the first one,  $RSE_2 = 0.0633$  for the second one, and  $RSE_3 = 0.0377$  for the third one. For the magnesium alloy in Figure 3.22,  $RSE_1 = 0.1079$  for the first one,  $RSE_2 = 0.2657$  for the second one and  $RSE_3 = 0.213$  for the third one. Apparently, the measurements with lower RSE indicate that the welding process is likely to run smoothly with less porosities. Based on experimental results, the “good welding” could be regarded as welding with RSE less than 0.05 for stainless steel and less than 0.15 for magnesium alloys.

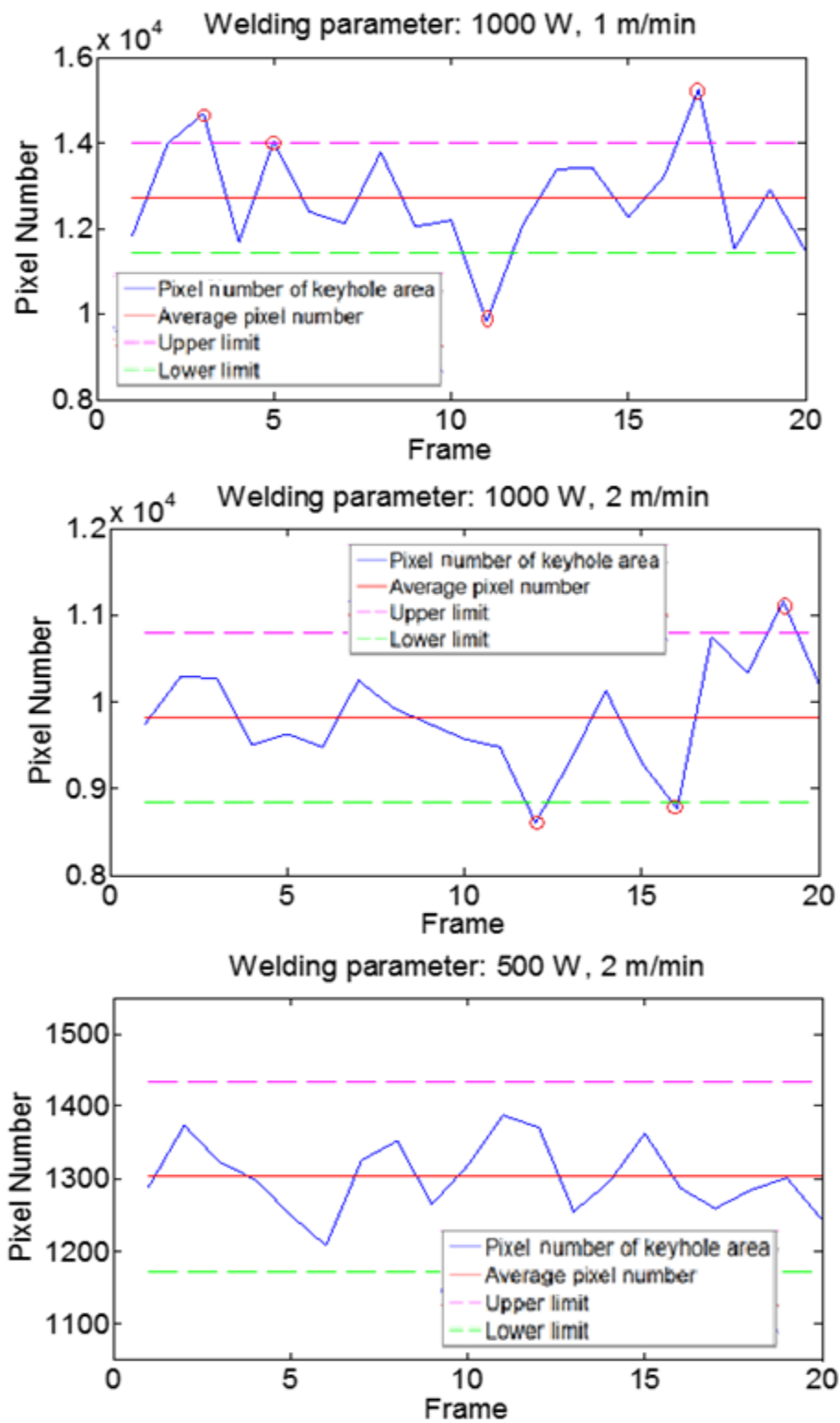


Figure 3.21. Detected keyhole sizes with stainless steel.

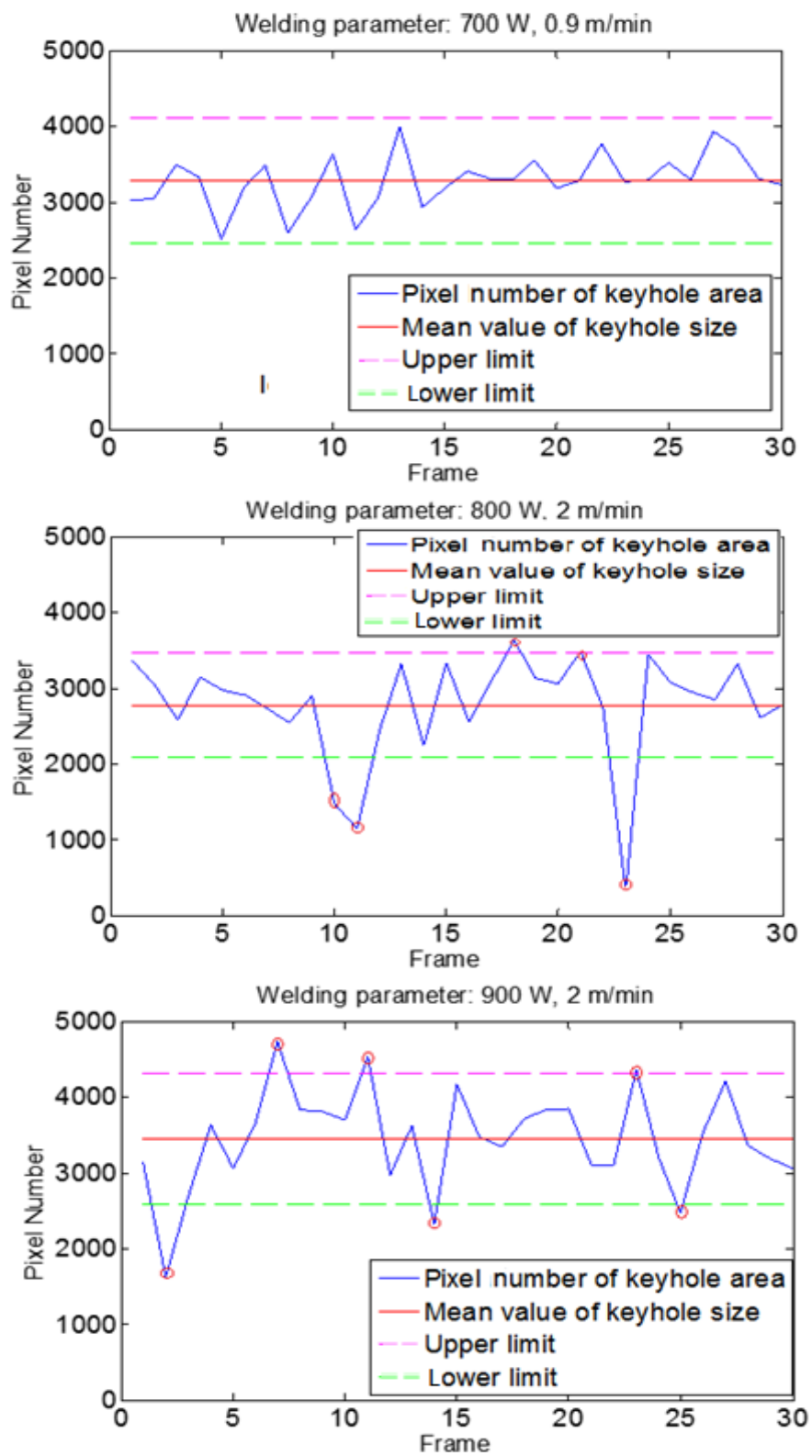


Figure 3.22. Detected keyhole sizes with magnesium alloys.

## CHAPTER 4. CONCLUSION AND RECOMMENDATION OF FUTURE WORK

### 4.1 Conclusion

In keyhole laser welding, the on-line weld pool monitoring plays a critical role in welding quality control. A coaxial monitoring system with a green laser illumination system was established to accurately detect the weld pool dynamics. Although the captured images still contained imaging noises, a complete weld pool boundary extraction algorithm was developed based on the local maximum gradient of greyness searching and linear interpolation, which efficiently resisted the potential imaging noises. Validation with the experimentally measured weld pool widths and predictions by the three-dimensional multi-phase model proved the effectiveness of the monitoring method. Another advantage is the potential for expansion of this work to multiple welding conditions with different base materials, such as stainless steel or magnesium alloys.

In addition, as keyhole dynamics significantly influence welding quality, the proposed static radial basis function neural network provides an accurate prediction of the major keyhole features with different welding conditions and measurements of the system based on the designed monitoring system. Under the changing welding parameters, the dynamic radial basis function neural network observer performs well in estimating the penetration depth and inclination angle. Additionally, the proposed approaches of porosity prediction, based on the visual monitoring system, successfully

indicate the occurrence of potential porosities in real-time experimentation.

To sum up, some major contributions could be generalized as follows:

- (1) Considering the cost and flexibility of our designed monitoring system, the whole system is more likely to be applied to the actual laser welding process in many industrial fields.
- (2) Use of the boundary extraction algorithm, static neural network and dynamic neural network-based state observer allow the dynamic three-dimensional keyhole geometry and weld pool edge to be captured without relying on complex measurement techniques and an accurate mathematic model.
- (3) The correlation between the change in keyhole size and potential welding defects is established so that a feedback welding control system can be designed.

#### 4.2 Recommendation of Future Work

As for the monitoring system, the green laser illumination works better with stainless steel than magnesium alloys (the weld pool geometry for stainless steel is much clearer) since the illumination source was selected in terms of the spectral analysis of plasma and plume on stainless steel. Although the extraction of the weld pool boundary is sufficient when using the proposed algorithms, other illumination sources, such as a red or blue laser, could be considered in order to improve the imaging quality of welding with magnesium alloys.

On the other hand, as has been mentioned above, more work with the controller design could be performed based on this well-established monitoring system. In particular, as the welding defects have been predicted in real time, welding speed and

laser power could be adjusted as inputs of the controller so that good welding quality can be guaranteed during the welding process.

In this work, the spectrometer is only used as a technique to analyze the spectra of plasma and plume. However, considering the advantages of high sampling rate and easy operation, more information about the weld pool could be obtained by collecting data from the spectrometer. Thus, the spectrometer and monitoring system can be combined together to provide the measurements for the control system. Moreover, through analysis of spectral data, a new mechanism of welding defect prediction can be set up as a validation for the approaches proposed in this work.



## LIST OF REFERENCES

## LIST OF REFERENCES

- [1] Na X (2010) Laser welding: techniques of real time sensing and control development, Laser Welding. Stone (Ed.) InTech.
- [2] Matsunawa A, Semak V (1997) The simulation of front keyhole wall dynamics during laser welding. *J Phys D Appl Phys* 30:798–809.
- [3] Lankalapalli KN, Tu JF, Gartner M (1996) Model for estimating penetration depth of laser welding processes. *J Phys D Appl Phys* 29:1831–41.
- [4] Lankalapalli KN, Tu JF, Leong KH, Gartner M (1999) Laser welding penetration estimation using temperature measurements. *J Manuf Sci Eng* 121(2):179–188.
- [5] Ye XH, Chen X (2002) Three-dimensional modelling of heat transfer and fluid flow in laser full-penetration welding. *J Phys D Appl Phys* 35:1049–56.
- [6] Ronda J, Siwek A (2011) Modelling of laser welding process in the phase of keyhole formation. *Archives of Civil and Mech Eng* 113:739–52.
- [7] Ki H, Mohanty P S, Mazumder J (2002) Modeling of laser keyhole welding: Part I. Mathematical modeling, numerical methodology, role of recoil pressure, multiple reflections, and free surface evolution. *Metall Mater Trans* 33A:1817–30.
- [8] Ki H, Mohanty P S, Mazumder J (2002) Modeling of laser keyhole welding: II. Simulation of keyhole evolution, velocity, temperature profile, and experimental verification. *Metall Mater Trans* 33A:1831–42.
- [9] Pang S, Chen L, Zhou J, Yin Y, Chen T (2011) A three-dimensional sharp interface model for self-consistent keyhole and weld pool dynamics in deep penetration laser welding. *J Phys D Appl Phys* 44:025301.
- [10] Zhao H, Niu W, Zhang B, Lei Y, Kodama M, Ishide T. Modelling of keyhole dynamics and porosity formation considering the adaptive keyhole shape and three phase coupling during deep-penetration laser welding. *J Phys D Appl Phys* 44:485302.

- [11] Tan W, Bailey NS, Shin YC (2013) Investigation of keyhole plume and molten pool based on a three-dimensional dynamic model with sharp interface formulation. *J Phys D Appl Phys* 46:055501.
- [12] Liu L, Hao X (2009) Improvement of laser keyhole formation with the assistance of arc plasma in the hybrid welding process of magnesium alloy. *Opt Laser Eng* 47:1177–82.
- [13] Shen X, Teng W, Huan W, Xu C (2013) Gas-jet-assisted Keyhole Laser Welding of Q235 Mild Steel. *Adv Mater Res* 629:180–6.
- [14] Sibillano T, Anconaa A, Berardia V, Schingaroc E, Basilea G, Lugara PM (2006) A study of the shielding gas influence on the laser beam welding of AA5083 aluminium alloys by in-process spectroscopic investigation. *Opt Laser Eng* 44:1039–51.
- [15] Li L (2002) A comparative study of ultrasound emission characteristics in laser processing. *Appl Surf Sci* 186:604–10.
- [16] Wang J, Yu H, Qian Y, Yang R (2011) Interference analysis of infrared temperature measurement in hybrid welding. Tarn TJ et al. (Eds.): *Robotic Welding, Intelligence and Automation*; LNEE 88:369–74.
- [17] Huang RS, Liu LM, Song G (2007) Infrared temperature measurement and interference analysis of magnesium alloys in hybrid laser-TIG welding process. *Mater Sci Eng* 447:239–43.
- [18] Kovacevic R, Zhang YM (1997) Real-time Image processing for monitoring of free weld pool surface. *Trans ASME J Manuf Sci Eng* 119(2):161–9.
- [19] Saeed G, Lou M, Zhang YM (2004) Computation of 3D weld pool surface from the slope field and point tracking of laser beams. *Meas Sci Technol* 15:389–403.
- [20] Song HS, Zhang YM (2007) Three-dimensional reconstruction of specular surface for a gas tungsten arc weld pool. *Meas Sci Technol* 18:3751–67.
- [21] Saeed G, Zhang YM (2007) Weld pool surface depth measurement using a calibrated camera and structured light. *Meas Sci Technol* 18:2570–8.
- [22] Kim C, Ah D. (2012) Coaxial monitoring of keyhole during Yb:YAG laser welding. *Opt Laser Technol* 44:1874–80.
- [23] Qin G, Qi X, Yang Y, Wang X, Lin S (2004) Acquisition and processing of coaxial image of molten pool and keyhole in Nd:Yag laser welding with high power, *China Welding* 13(1):51–5.

- [24] Zhang Y, Zhang C, Tan L, Li S (2013) Coaxial monitoring of the fiber laser lap welding of Zn-coated steel sheets using an auxiliary illuminant. *Opt Laser Technol* 50:167–75.
- [25] Gao J, Qin G, Yang J, He J (2011) Image processing of weld pool and keyhole in Nd:YAG laser welding of stainless steel based on visual sensing. *Nonferrous Met Soc China* 21:423–8.
- [26] Fabbro R (2010) Melt pool and keyhole behaviour analysis for deep penetration laser welding. *J Phys D Appl Phys* 43:445501.
- [27] Fabbro R, Slimani S, Coste F, Briand F (2005) Study of keyhole behavior for full penetration Nd–Yag CW laser welding. *J Phys D Appl Phys* 38:1881–7.
- [28] Fabbro R, Slimani S, Doudet I, Coste F, Briand F (2006) Experimental study of the dynamical coupling between the induced vapor plume and the melt pool for Nd–Yag laser welding. *J Phys D App Phys* 39:394–400.
- [29] Kawahito Y, Mizutani M, Katayama S (2007) Investigation of high-power fiber laser welding phenomena of stainless steel. *Tran JWRI* 362:11–6
- [30] Wahba M, Katayama S (2012) Laser welding of magnesium alloys. *Tran JWRI* 411: 11–23.
- [31] Katayama S, Mizutani M, Matsunawa A (2003) Development of porosity prevention procedures during laser welding. *Proc SPIE* 4831:281–8.
- [32] Seto N, Katayama S, Matsunawa A (2000) High-speed simultaneous observation of plasma and keyhole behavior during high power CO<sub>2</sub> laser welding: Effect of shielding gas on porosity formation. *J Laser Appl* 12:245–50.
- [33] Kaplan AFH, Mizutani M, Matsunawa A, Katayama S (2002) Unbounded keyhole collapse and bubble formation during pulsed laser interaction with liquid zinc. *J Phys D Appl Phys* 35:1218–28.
- [34] Lu S, Basar T (1998) Robust nonlinear system identification using neural-network models. *IEEE Tran Neural Netw* 93:407–29.
- [35] Xu H, Chowdhury FN (2007) Neural networks based system identification techniques for model based fault detection of nonlinear systems. *Int J Innov Comput Info Contr* 35:1073–1085.
- [36] Ranković VM, Nikolić LZ (2008) Identification of nonlinear models with feedforward neural network and digital recurrent network. *FME Tran* 36:87–92.

[37] Kalman RE (1960) A New Approach to Linear Filtering and Prediction Problems. *J Basic Eng* 82(D):35–45.

[38] Jazwinski AH (1970) *Stochastic process and filter theory*. New York: Academic Press.

[39] Norgaard M, Poulsen NK, Ravn O (2000) New developments in state estimation for nonlinear systems, *Automatica* 36:1627–1638.

[40] Subrahmanya N, Shin YC (2009) Adaptive divided difference filtering for simultaneous state and parameter estimation. *Automatica* 45:1686–1693.

[41] Elanayar S, Shin YC (1994) Radial basis function neural network for approximation and estimation of nonlinear stochastic dynamic systems. *IEEE Tran Neural Netw* 54:594–603.

[42] Elanayar S, Shin YC (1995) Robust tool wear estimation with radial basis function neural networks. *J Dyn Control Syst* 117:459–67.

[43] Lee CW, Shin YC (2003) Construction of fuzzy systems using least-squares method and genetic algorithm. *Fuzzy Sets Syst* 137:297–323.

VITA

## VITA

Masiyang Luo

School of Mechanical Engineering, Purdue University

Masiyang Luo receives his Bachelor of Science in Electronic and Computer Engineering in June of 2011 from Beijing Institute of Technology in Beijing, China. Beginning in August of 2012, he started his graduate studies in the School of Mechanical Engineering at Purdue University. His research interests include intelligent control in laser-based manufacturing, system identification, keyhole dynamic analysis and imaging processing for weld pool monitoring.